



Evaluating soil moisture retrieval in Arctic and sub-Arctic environments using passive microwave satellite data

Juliette Ortet, Arnaud Mialon, Yann Kerr, Alain Royer, Aaron Berg, Julia Boike, Elyn Humphreys, François Gibon, Philippe Richaume, Simone Bircher-Adrot, Azza Gorraab & Alexandre Roy

To cite this article: Juliette Ortet, Arnaud Mialon, Yann Kerr, Alain Royer, Aaron Berg, Julia Boike, Elyn Humphreys, François Gibon, Philippe Richaume, Simone Bircher-Adrot, Azza Gorraab & Alexandre Roy (2024) Evaluating soil moisture retrieval in Arctic and sub-Arctic environments using passive microwave satellite data, International Journal of Digital Earth, 17:1, 2385079, DOI: [10.1080/17538947.2024.2385079](https://doi.org/10.1080/17538947.2024.2385079)

To link to this article: <https://doi.org/10.1080/17538947.2024.2385079>



© 2024 The Author(s). Published by Informa UK Limited, trading as Taylor & Francis Group



[View supplementary material](#)



Published online: 04 Aug 2024.



[Submit your article to this journal](#)



Article views: 442



[View related articles](#)



[View Crossmark data](#)

Evaluating soil moisture retrieval in Arctic and sub-Arctic environments using passive microwave satellite data

Juliette Ortet ^{a,b,c}, Arnaud Mialon ^b, Yann Kerr ^b, Alain Royer ^d, Aaron Berg ^e, Julia Boike ^{f,g}, Elyn Humphreys ^h, François Gibon ^b, Philippe Richaume ^b, Simone Bircher-Adrot ⁱ, Azza Gorraab ^{a,c} and Alexandre Roy ^{a,c}

^aDépartement des sciences de l'environnement, Université du Québec à Trois-Rivières, Quebec, Canada; ^bCentre d'Etudes Spatiales de la Biosphère, CESBIO Université de Toulouse (CNES/CNRS/INRAE/IRD/UT3), Toulouse, France; ^cCentre d'études nordiques, Québec, Quebec, Canada; ^dDépartement de géomatique appliquée, Université de Sherbrooke, Sherbrooke, Canada; ^eDepartment of Geography, Environment and Geomatics, University of Guelph, Guelph, Ontario, Canada; ^fAlfred Wegener Institute (AWI), Helmholtz Centre for Polar and Marine Research, Potsdam, Germany; ^gGeography Department, Humboldt-Universität zu Berlin, Berlin, Germany; ^hDepartment of Geography & Environmental Studies, Carleton University, Ottawa, Ontario, Canada; ⁱMeteo Swiss, Payerne, Switzerland

ABSTRACT

Soil Moisture (SM) is a key parameter in northern Arctic and sub-Arctic (A-SA) environments that are highly vulnerable to climate change. We evaluated six SM satellite passive microwave datasets using thirteen ground-based SM stations across Northwestern America. The best agreement was obtained with SMAP (Soil Moisture Active Passive) products with the lowest RMSD (Root Mean Square Difference) ($0.07 \text{ m}^3 \text{ m}^{-3}$) and the highest R (0.55). ESA CCI (European Space Agency Climate Change Initiative) also performed well in terms of correlation with a similar R (0.55) but showed a strong variation among sites. Weak results were obtained over sites with high water body fractions. This study also details and evaluates a dedicated retrieval of SM from SMOS (Soil Moisture and Ocean Salinity) brightness temperatures based on the $\tau - \omega$ model. Two soil dielectric models (Mironov and Bircher) and a dedicated soil roughness and single scattering albedo parameterization were tested. Water body correction in the retrieval shows limited improvement. The metrics of our retrievals ($\text{RMSD} = 0.08 \text{ m}^3 \text{ m}^{-3}$ and $R = 0.41$) are better than SMOS but outperformed by SMAP. Passive microwave satellite remote sensing is suitable for SM retrieval in the A-SA region, but a dedicated approach should be considered.

ARTICLE HISTORY



Received 1 March 2024
Accepted 22 July 2024

KEYWORDS

Arctic and sub-Arctic; CCI; L-band; SMAP; SMOS; soil moisture

1. Introduction

Soil Moisture (SM) is the amount of water stored in the unsaturated soil layer (Seneviratne et al. 2010). In 2010, the GCOS (Global Climate Observing System) classified SM as an essential climate variable as it is an integral and dynamic part of the hydrological cycle (Wagner et al. 2012). At global, regional and local scales, SM takes part in multiple aspects of the soil–vegetation–atmosphere

CONTACT Juliette Ortet  juliette.ortet@uqtr.ca  Département des sciences de l'environnement, Université du Québec à Trois-Rivières, Trois-Rivières, Quebec G9A 5H7, Canada; Centre d'Etudes Spatiales de la Biosphère, CESBIO Université de Toulouse (CNES/CNRS/INRAE/IRD/UT3), Toulouse 31401, France; Centre d'études nordiques, Québec, Quebec G1V 0A6, Canada

© 2024 The Author(s). Published by Informa UK Limited, trading as Taylor & Francis Group
This is an Open Access article distributed under the terms of the Creative Commons Attribution-NonCommercial License (<http://creativecommons.org/licenses/by-nc/4.0/>), which permits unrestricted non-commercial use, distribution, and reproduction in any medium, provided the original work is properly cited. The terms on which this article has been published allow the posting of the Accepted Manuscript in a repository by the author(s) or with their consent.

interaction and is highly impacted by climate change (Berg and Sheffield 2018; Seneviratne et al. 2010). In the Arctic and sub-Arctic (hereafter called A-SA) regions, water resources vary and impact both fauna and flora. For example, Ackerman et al. (2017) and Zona et al. (2023) showed that the SM decrease associated with temperature increase may limit vegetation growth in tundra environments. Hence, the carbon cycle in the A-SA area is highly sensitive to SM changes in the active layer of the permafrost (Falloon et al. 2011; Lawrence et al. 2015). The future of SM in permafrost regions and its impact on carbon–climate feedbacks remains unclear as climate models disagree when predicting the hydrological regime in these regions (Andresen et al. 2020). Accurately monitoring SM is thus essential despite the challenges related to the SM strong temporal and spatial variability in these regions (Ochsner et al. 2013).

Remote sensing of SM has shown great potential at L-band (typical frequency = 1400–1427 GHz, wavelength $\lambda \simeq 21$ cm). Passive microwave remote sensing consists in measuring the earth's microwave emissions as brightness temperature (TB). The microwave emission at L-band is highly sensitive to liquid water in soil and vegetation because of the high dielectric constant of water (Ulaby, Moore, and Fung. 1981). At the same time, it is sensitive to the effective soil temperature, the surface roughness and the above-ground vegetation. All these interactions must be considered in a Radiative Transfer Model (RTM). The $\tau - \omega$ model accounts for vegetation effects, both attenuation and emission, due to transmissivity (optical depth -- τ) and scattering (effective single scattering albedo - ω) (Mo et al. 1982). The signal's estimated soil penetration depth is generally associated with the top 5 cm (Schmugge 1983), but some studies estimated a smaller (e.g. 2 cm) or larger (e.g. 10 cm) depth as the signal penetration varies according to the SM content and soil characteristics (Escorihuela et al. 2010; Lv et al. 2018). Passive microwave satellites follow a sun-synchronous orbit and have a high temporal revisit frequency of three days at the equator. The temporal resolution improves with latitude, reaching an optimum of multiple passes per day over the A-SA regions. SMOS (Soil Moisture and Ocean Salinity) and SMAP (Soil Moisture Active Passive) satellite missions are operating at L-band frequency and provide several SM global datasets. ESA CCI (European Space Agency Climate Change Initiative) also processes several SM datasets resulting in merged SM datasets: active only, passive only and merged active–passive.

However, none of these products offers dedicated parameterization for A-SA regions and sufficient validation is still lacking in these regions. The many water bodies in these regions lead to difficulties in SM retrievals with passive microwave observations. Water bodies such as lakes and rivers or coastal territories cover a huge part of the northern regions in North America (Pekel et al. 2016). High spatial heterogeneity in the large passive microwave satellite footprint (~ 40 km²) and the low TB emissions for water bodies hinder SM retrieval (Kerr et al. 2010). Also, soils in A-SA environments generally contain higher contents of organic matter, implying specific water storage and drainage systems (Bakian-Dogaheh et al. 2022; Rawls et al. 2003), which further impacts the L-band signal (Yi et al. 2022). Finally, tundra vegetation is variable and dynamic in a climate change context (Myers-Smith et al. 2020), but its interaction with microwave emissions is not well quantified.

This study aims to investigate the performance of satellite-based passive microwave SM retrievals over A-SA environments in Northwestern North America. The first objective is to evaluate several SM datasets (SMOS, SMAP, ESA CCI) by comparing with *in situ* measurements. The second objective aims at adapting an RTM and an inversion approach to improve SM retrieval over A-SA environments. More specifically, we considered three important components of the SM retrieval in A-SA environments: (1) accounting for water bodies in our simple retrieval approach, (2) finding an adequate soil dielectric constant, (3) improving the single scattering albedo (ω) and soil roughness (H_r) parameterization and assess their impact on SM retrievals. Finally, we compared SM obtained with the new parameterization with the evaluated satellite and with *in situ* SM datasets.

2. Materials

2.1. In situ dataset

In this study, we gathered several measurements to establish an *in situ* SM database over the A-SA region (Figure 1 and Table 1). *In situ* SM measurements include data from across Canada and Alaska (USA) based on accessibility and environmental conditions. The *in situ* dataset mainly comes from the open-access International Soil Moisture Network (ISMN) (Dorigo et al. 2021) database. It provides SM measurements over several stations in Northern America. The few SM stations in the A-SA are provided mostly by the SNOTEL (Snowpack Telemetry) (Leavesley et al. 2010) network. Eleven of the thirteen sites of this study are part of this network providing SM at different depths in the soil horizon using Hydra Probe sensors (Table 1). The SNOTEL *in situ* SM measurements are not derived using a calibration for organic material, but rather using the probes' factory calibration. Datasets from Trail Valley Creek (Northwest Territories, Canada) (Boike et al. 2023) and Daring Lake (Northwest Territories, Canada) stations completed our data (Lafleur and Humphreys 2018). For Trail Valley Creek, SM is derived from relative permittivity measurements with a Time Domain Reflectometry (TDR) Campbell Scientific CS630 probe and using a mixing model not dedicated to organic soils (Boike et al. 2018). The Daring Lake site is monitored at eight locations using Campbell Scientific CS616 probes based on no soil-specific calibration. L-band is mainly sensitive to the surface soil layer, hence only measurements conducted at a depth of 5 cm or 2 in (i.e. 5.08 cm) in the soil were considered. These measurements are widely used to validate L-band remote sensing data (Gruber et al. 2020) as they provide the best match between the soil volume



Figure 1. Distribution of the 13 ground-based SM stations network used as reference in this study (background: ESA CCI L4 map at 300 m, Version 2.0.7 (2015) ESA 2017). Coordinates location is specified in Table 1.

Table 1. Locations and availability of the study ground-based SM stations.

Site	Latitude (in °)	Longitude (in °)	Date period	Reference
Imnaviat Creek	68.62	-149.30	2010.10.24–2019.10.14	Leavesley et al. (2010)
Atigun Pass	68.13	-149.48	2007.08.08–2019.11.22	Leavesley et al. (2010)
Coldfoot	67.25	-150.18	2005.03.09–2021.07.30	Leavesley et al. (2010)
Gobblers Knob	66.75	-150.67	2006.10.01–2019.10.14	Leavesley et al. (2010)
Eagle Summit	65.49	-145.41	2006.10.01–2019.10.14	Leavesley et al. (2010)
Mt Ryan	65.25	-146.15	from 2011.10.04	Leavesley et al. (2010)
Kelly Station	67.93	-162.28	from 2011.07.22	Leavesley et al. (2010)
Aniak	61.58	-159.58	2012.09.21–2019.10.14	Leavesley et al. (2010)
Little Chena Ridge	65.12	-146.73	from 2011.10.04	Leavesley et al. (2010)
Monument Creek	65.08	-145.87	from 2011.10.24	Leavesley et al. (2010)
Munson Ridge	64.85	-146.21	from 2011.10.17	Leavesley et al. (2010)
Trail Valley Creek	68.75	-133.50	2016.08.27–2019.08.02	Boike et al. (2023)
Daring Lake	64.87	-111.58	2010.01.01–2023.05.01	Lafleur and Humphreys (2018)

measured by a probe and the penetration depth of L-band among the few *in situ* SM measurements available. The sites investigated in this study are representative of high-latitude regions. These regions are quite challenging for SM estimates due to water bodies and high organic soil content. Sites with flat topography were selected to ensure the low impact of topography on L-band measurements (Kerr et al. 2003; Mialon et al. 2008). Section 3.1 details the method for processing the measurements time series.

2.2. Satellite SM datasets

Table 2 sums up the main characteristics of the satellite SM datasets used in this study. In this paper, morning (AM) and afternoon (PM) orbits are considered separately for each satellite product, as they differ significantly due to diurnal hydrological variations (Kerr et al. 2016). Section 3.1 details the data filtering procedure.

2.2.1. SMOS

On November 2, 2009, the European Space Agency (ESA) launched the SMOS satellite. Its payload consists of 69 elementary antennas arranged on a Y-shaped structure. SMOS is on a near-polar sun-synchronous orbit with ascending/descending passes at 6 a.m./6 p.m. and a temporal resolution of twice every three days at the equator. For each overpass, several observations are acquired over a range of incidence angles. In A-SA, the revisit time of a satellite with a near-polar orbit is much shorter (up to 10 times per day). Consequently, in this study, we have at least one SM retrieval per day. The overpass time of the SMOS satellite in A-SA is not exactly the same as for the equator, but rather at 7 a.m./9 p.m. The retrieval accuracy in the morning and the afternoon may vary because of different temperature gradients. Radio Frequency Interferences (RFI) also impact differently ascending and descending passes.

The SMOS Level 3 (L3) brightness temperatures are top-of-atmosphere TB provided in vertical (*V*) and horizontal (*H*) polarizations (Al Bitar et al. 2017). For our retrievals specifically adapted to

Table 2. Grids and temporal samplings of the satellite SM datasets.

	Grid	Grid sampling	Temporal sampling
SMAP L3 P	EASE 2.0 grid, Global	36 km	6 a.m. and 6 p.m.
SMAP L3 PE	EASE 2.0 grid, Global	9 km	6 a.m. and 6 p.m.
SMOS L2	ISEA4-9 grid, Global	15 km	6 a.m. and 6 p.m.
SMOS L3	EASE 2.0 grid, Global	25 km	6 a.m. and 6 p.m.
SMOS-IC	EASE 2.0 grid, Global	25 km	6 a.m. and 6 p.m.
CCI	0.25° regular grid	0.25°	Daily mean

A-SA environments, we used the SMOS Level 3 TB version 330 (Cabot 2016), sampled on the global (Equal Area Scalable Earth) EASE 2.0 grid obtained from the Centre Aval de Traitement des Données SMOS (CATDS). Our SM retrieval process was based on the daily nominal dataset with both H and V polarizations and for both ascending and descending orbits. The L3 TB are provided for specific observation angles θ from 0° to 55° binned over 5-degree intervals; each 5-degree angle bin contains averaged multi-angular measurements. Besides H and V TB values for each grid point, the L3 TB datasets provide pixel radiometric accuracy and RFI flags that may be used to filter the satellite measurements before the inversion. However, there are very few RFI in the A-SA region except before May 2012 (Aksoy and Johnson 2013) and after 2023, which are not considered in our study.

SMOS official retrieval products are based on the L-MEB (L-band Microwave Emission of the Biosphere) model as a 0th-order Radiative Transfer Model (RTM). L-MEB includes the $\tau - \omega$ model, which accounts for vegetation effects, parameterized by the optical depth τ and the single scattering albedo ω . In a 2-parameter approach, the SMOS inversion simultaneously retrieves the SM and the Vegetation Optical Depth (VOD), assuming they are the same at both polarizations.

In this study, we compared different SM satellite datasets. For SMOS, the three datasets used are the ESA SMOS L2 SM v700 (2021), the CATDS SMOS L3 SM v338 (CATDS 2016) and the SMOS-IC v2 (Wigneron et al. 2021) datasets. The SMOS L2 SM v700 are delivered for half orbit on the Icosahedron Snyder Equal Area (ISEA) Aperture 4 Hexagonal (ISEA4H) (Talone et al. 2015) grid system having a sampling of ≈ 15 km internodes' distances (Kerr et al. 2012). The land cover used to produce the SMOS L2 SM v700 is a simplified version of the International Geosphere-Biosphere Programme (IGBP) classification (Broxton et al. 2014). The SMOS L3 SM v338 dataset is sampled on the EASE 2.0 global grid of 25 km sampling at 30° latitude. Note that the SMOS Level 3 operational algorithm is based on the Level 2 algorithm with a few changes: it includes temporal processing (Al Bitar et al. 2017). The SMOS-IC (SMOS-INRA-CESBIO) v2 dataset results from the inversion of the SMOS Level 3 TB. SMOS-IC SM are provided on same grid as the SMOS L3 SM dataset: the EASE 2.0 global grid with a sampling at 25 km at 30° latitude. In the SMOS-IC algorithm, the basic concept is the same as for L2 with the exception that each pixel is considered homogeneous (a single $\tau - \omega$ model is applied). Look-Up Tables (LUT) and auxiliary datasets are used with calibrated vegetation and soil parameters for different land cover classes (Wigneron et al. 2021). Note that even if the sampling grids may differ depending on the products, the basic native resolution is always the same at ~ 40 km.

2.2.2. SMAP

The SMAP satellite was launched by the National Aeronautics and Space Administration (NASA) on January 31, 2015. An L-band radiometer and a synthetic aperture radar were on board, but unfortunately the latter faced an irrevocable failure on July 7, 2015. Similarly to SMOS, the SMAP satellite follows a polar near-sun-synchronous orbit which enables an equivalent revisit time of two to three days but the ascending/descending passes are opposite at 6 p.m./6 a.m. (i.e. around 9 a.m./7 p.m. in northern A-SA). The radiometer has a fixed incidence angle of 40° .

The SMAP SM retrieval algorithm currently uses the Dual Channel Algorithm (DCA) (Chaubell et al. 2020), which considers brightness temperatures in H and V polarizations from the SMAP Level 1B Brightness Temperature dataset (L1BTB). Radiative transfer equations used for SMAP are very similar to those of the SMOS algorithm (L-MEB and $\tau - \omega$). Each pixel is considered as a uniform surface. In the official SMAP retrieval products, the Normalized Difference Vegetation Index (NDVI) allows establishing a linear relationship with the vegetation water content and a vegetation opacity estimation to finally retrieve SM and VOD simultaneously (O'Neill, Bindlish et al. 2021). In this study, the two considered SMAP gridded datasets are SMAP L3 SM P (Soil Moisture Active Passive L3 Soil Moisture Passive) Version 8 (O'Neill, Chan, Njoku, Jackson, Bindlish and Chaubell 2021) and SMAP L3 SM PE (Soil Moisture Active Passive L3 Soil Moisture Passive Enhanced) Version 5 (O'Neill, Chan, Njoku, Jackson, Bindlish, Chaubell and Colliander 2021).

The SMAP L3 SM P Version 8 dataset O'Neill, Chan, Njoku, Jackson, Bindlish and Chaubell (2021) is a daily global composite obtained from the half-orbit SMAP L2 SM P dataset. The SMAP L3 datasets are daily global maps that also contain several inversion static auxiliary data (e.g. radar water fraction or land cover). The SMAP L3 SM P dataset grid is the 36 km global EASE 2.0 grid (Brodzik et al. 2012), which is close to the native radiometer resolution of ~ 40 km. Composite datasets are obtained by reconstructing TB for each pixel of the grid. The global EASE 2.0 grid preserved the areas (here, $36 \times 36 \text{ km}^2$), rather than the distances, so the shape of the pixels varies from one site to another along the latitudes. It results in a higher vertical length at the poles and raises the issue of the representativeness of such shaped pixels as the SMAP acquisitions are resampled to the EASE 2.0 grid pixel shape (Wrona et al. 2017). A precise consideration of the pixel area is crucial to account for water fraction contributions in the resulting TB.

SMAP also provides an enhanced interpolation of the original SMAP Level 1B Brightness Temperature dataset (L1B TB) providing a higher spatial sampling. Similarly to the SMAP L2 SM P official product, a SMAP L2 SM PE passive dataset is computed and to obtain the SMAP L3 SM PE Version 5 official product (O'Neill, Chan, Njoku, Jackson, Bindlish, Chaubell and Colliander 2021). For the SMAP Enhanced L3 SM dataset (Chan and Dunbar 2021), the TB are over-sampled to the 9 km global EASE 2.0 grid (Brodzik et al. 2012), though the measurements are still provided by an instrument of ~ 40 km resolution. For homogeneous areas, the satellite dataset's agreement with *in situ* measurements remains correct when using a finer grid, as Colliander et al. (2018) and Madelon et al. (2023) indicate. However, significant differences may arise for heterogeneous areas if the radiometer resolution is higher than the sampling grid.

2.2.3. CCI SM

The ESA CCI SM dataset (hereafter called CCI) is the first long-term global SM dataset derived from satellite data. Meeting the requirements of Climate Data Records (CDR) datasets, it provides daily SM for more than 40 years on a 0.25° regular grid. Its extensive temporal and spatial resolutions are ensured by the combination of microwave SM retrievals obtained from both active and passive sensors (Dorigo et al. 2017). The SM retrievals rely on the Land Parameter Retrieval Model (LPRM) (Owe, De Jeu, and Holmes 2008) for passive sensors and the TU-Wien change detection method (Naeimi et al. 2009; Wagner, Lemoine, and Rott 1999) for active sensors. Based on their respective error characteristics, the obtained PASSIVE and ACTIVE products are merged into a COMBINED product (Dorigo et al. 2017), obtained from up to ten microwave sensors (including SMOS and SMAP), operating over frequencies from 1.4 GHz to 19.4 GHz (Gruber et al. 2019). We use the COMBINED Version 08.1 dataset (Dorigo et al. 2023) consisting of a daily dataset provided on a grid with a 0.25° regular longitude/latitude spacing.

2.3. Other datasets

2.3.1. Land cover

The performance of the SM datasets over the study sites is investigated in relation to the land cover (Table 3), as the latter impacts the retrieved SM. The land cover fraction is obtained from the ESA CCI L4 map at 300 m, Version 2.0.7 (2015) (ESA 2017) using a 40 km diameter buffer zone around each SMOS L3 node. This roughly corresponds to a 3 dB cut-off that accounts for the instrumental resolution at L-band. To help the analysis, we gather the study sites into study groups based on the major land covers found within the 40 km buffer zone. For most sites, the water fraction is under 10%, but for Trail Valley Creek and Daring Lake sites, the water fraction is above 30% (see Appendix). Since water bodies significantly impact TB measurements and thus SM retrieval at L-band (Kerr et al. 2012), both Trail Valley Creek and Daring Lake were assigned to a dedicated study group ('*HighWF*' group). The vegetation interactions with passive microwave emissions cannot be ignored, that is why the other groups depend on the vegetation type. '*SpVeg*' stands for sparse vegetation and encompasses sites with high fractions of the classes Grassland, Lichen and Mosses

Table 3. Study sites land cover fractions extracted from the ESA CCI L4 map at 300 m, Version 2.0.7 (2015) (ESA 2017) using a 40 km diameter buffer around each SMOS L3 node. Study groups are established based on the major land covers in the site environment.

Study group	Site	Tr.n.(15) ¹	Tr.n.(40) ²	Tr.m. ³	Tr.Sh.(50) /He(50) ⁴	Sh. ⁵	Gr. ⁶	Li.Mo. ⁷	S.v.(15) ⁸	W. ⁹
<i>SpVeg</i>	Imnaviat Creek	0.00	0.00	0.00	0.00	0.01	0.24	0.02	0.71	0.01
	Atigun Pass	0.01	0.01	0.00	0.00	0.02	0.03	0.34	0.33	0.01
	Coldfoot	0.19	0.05	0.05	0.11	0.35	0.09	0.01	0.10	0.00
	Gobblers Knob	0.23	0.09	0.01	0.14	0.31	0.04	0.01	0.16	0.00
<i>Shrub</i>	Eagle Summit	0.15	0.04	0.00	0.15	0.38	0.09	0.00	0.17	0.00
	Mt Ryan	0.21	0.08	0.00	0.19	0.29	0.08	0.01	0.14	0.00
	Kelly Station	0.05	0.02	0.00	0.03	0.42	0.15	0.09	0.09	0.03
	Aniak	0.04	0.02	0.14	0.09	0.26	0.18	0.00	0.04	0.08
<i>TreeCov</i>	Little Chena Ridge	0.19	0.49	0.19	0.01	0.05	0.01	0.00	0.02	0.00
	Monument Creek	0.20	0.49	0.09	0.07	0.08	0.01	0.01	0.03	0.00
<i>HighWF</i>	Munson Ridge	0.18	0.47	0.14	0.06	0.09	0.01	0.00	0.03	0.00
	Trail Valley Creek	0.04	0.01	0.00	0.02	0.27	0.08	0.03	0.14	0.42
	Daring Lake	0.03	0.02	0.00	0.01	0.00	0.00	0.21	0.38	0.36

¹ Tree cover needleleaved evergreen closed to open (> 15%).

² Tree cover needleleaved evergreen closed (> 40%).

³ Tree cover mixed leaf type (broadleaved and needleleaved).

⁴ Mosaic tree and shrub (> 50%) / herbaceous cover (< 50%).

⁵ Shrubland.

⁶ Grassland.

⁷ Lichens and mosses.

⁸ Sparse vegetation (tree shrub herbaceous cover) (< 15%).

⁹ Water bodies.

and Sparse vegetation. ‘*TreeCov*’ groups the sites whose major ESA CCI classes imply high tree coverage. ‘*Shrub*’ group gathers the sites dominated by the ESA CCI Shrubland class fraction. No permanent snow nor ice conditions appear according to ESA CCI L4 map.

2.3.2. Soil properties

SM retrieval performances should be interpreted with respect to soil properties, as the dielectric model considers it in the retrieval process. In the RTM used in this study (see Section 3.3), the soil dielectric model requires the clay content fraction as input. The various soil property information (clay fraction, sand fraction, soil organic content, and bulk density) are extracted from SoilGrids 250 m v2.0 (Poggio et al. 2021) for the 0–5 cm soil layer (Table 4). Similarly to the land cover, a 40 km diameter buffer is considered around each SMOS L3 node. The study sites appear to be quite homogeneous, with high Soil Organic Carbon (SOC) content with respect to the SoilGrid

Table 4. Study sites soil characteristics at 0–5 cm for a 40 km diameter buffer around each SMOS L3 node extracted from SoilGrids.

Study group	Site	Clay (%)	Sand (%)	SOC (g kg ⁻¹)	Bulk density (g cm ⁻³)
<i>SpVeg</i>	Imnaviat Creek	15.8	35.0	262.3	0.39
	Atigun Pass	16.3	32.8	185.0	0.46
	Coldfoot	10.1	31.5	199.5	0.42
	Gobblers Knob	9.6	26.9	204.7	0.40
<i>Shrub</i>	Eagle Summit	10.1	28.9	231.0	0.36
	Mt Ryan	10.2	21.3	195.9	0.29
	Kelly Station	9.3	24.9	228.4	0.30
	Aniak	10.5	29.1	238.4	0.33
<i>TreeCov</i>	Little Chena Ridge	9.5	24.1	220.8	0.28
	Monument Creek	13.1	25.7	229.4	0.43
<i>HighWF</i>	Munson Ridge	6.6	18.7	180.0	0.50
	Trail Valley Creek	14.9	13.2	51.0	0.31
	Daring Lake	6.1	27.2	44.0	0.34

250 m v2.0 mean at global scale ($\simeq 40 \text{ g kg}^{-1}$) (Poggio et al. 2021). The sites from the ‘*HighWF*’ group have the lower SOC content ($\simeq 50 \text{ g kg}^{-1}$, i.e. four times lower than that of the other sites mean value). While Trail Valley Creek has the lowest percentage of sand, Daring Lake has the lowest clay percentage.

2.3.3. Scene physical temperatures

The SMOS L3 TB ECMWF (European Centre for Medium-Range Weather Forecasts) auxiliary data contains various surface variables, such as surface physical temperatures, provided on the same EASE 2.0 global grid with an interpolation at the exact satellite overpass time. Soil temperatures at 0–7 cm and 28–100 cm depths are respectively used as soil surface and deep temperatures. The canopy temperature is assumed to be similar to the air temperature at 2 m above the ground. In this study, in addition to soil and air temperatures, we needed to define the water bodies’ physical temperature to be able to include their contribution to the TB. We assumed that water bodies’ physical temperature were equal to the sea surface temperature provided by ECMWF. After testing our model’s sensibility, variations of a few K in the ECMWF surface temperatures were negligible in the inversion process. We also noticed that ECMWF surface temperatures were quite close to the *in situ* ones at each site.

3. Methods

In this study, we first compared the existing SM datasets and evaluated their performance over all sites. Then, we tested four configurations of RTM for water body fraction and soil dielectric model to retrieve SM from SMOS L3 TB. Finally, we optimized the parametrization of the single scattering albedo (ω) and surface roughness (H_r) over the sites.

3.1. Data processing

For each site, we considered one probe and one satellite footprint. At Daring Lake, we considered the mean value of all the 8-probe network measurements (Gruber et al. 2020; Jackson et al. 2010). Each site included an *in situ* instrument that measures SM at 5 cm depth, with measurements routinely acquired every hour (except for periods when sensors failed). ISMN flags with ‘G’ the data considered of good quality. The availability of both *in situ* and satellite data defined the period covered by this study. SMOS and SMAP satellites provided us with SM datasets from 2010 and 2015 respectively, whereas *in situ* measurements for most previously selected sites end in 2019. Our study spans from 2015 to 2019. The *in situ* datasets were filtered considering meteorological conditions, as snow and frozen ground make the SM retrievals uncertain. Consequently, we only kept summertime data (no snow cover, unfrozen soil and positive air temperature, based on available data from sites’ additional sensors). For all the sites, summertime encompasses at least the July–August period, and depending on the site, it extends from mid-May to end of October. Each SM satellite retrieval was compared to the nearest *in situ* measurement. Satellite data with an absolute time difference exceeding 30 minutes between the satellite and *in situ* probe measurements was discarded as suggested by Montzka et al. (2021).

The SM values (expressed as $\text{m}^3 \text{ m}^{-3}$) were restricted to the $[0, 1]$ range, and each satellite dataset was filtered following their respective quality control flags. For SMAP L3 P and PE, high quality is considered with a retrieval quality flag set to 0 or 8 (Chan and Dunbar 2021; O’Neill, Bindlish et al. 2021). ESA CCI dataset only provides SM values when no data inconsistency is detected, i.e. a flag value of 0 or 8 (the latter accounting for barren ground). Both SMOS L2 and SMOS L3 contain a RFI probability obtained from past RFI events detected for each SMOS node. Additionally, both datasets encompass a Chi2 probability value for each SM that accounts for the fit quality, from modeled TB versus SMOS observed TB (Kerr et al. 2020). SM retrievals were only kept when $\text{RFI Prob} < 0.1$ and $\text{Chi 2 Prob} > 0.05$. In the case of SMOS-IC, a threshold value of 8 K was applied to the Root Mean

Square Error (RMSE) value between the measured and the modeled TB data (Wigneron et al. 2021). As for the SMOS L3 TB dataset used in our enhanced retrieval process, all the TB bins with mean angles from 0 to 60° with a 5° step were considered. TB data with an RFI ratio (which corresponds to the sum of the RFI flag divided by the sum of the satellite views) above 0.1 were discarded.

3.2. Metrics

The *in situ* measurement dynamics were evaluated using:

- the mean value (mean) of an SM time series:

$$SM_{\text{mean}} = \frac{1}{n} \sum_{i=1}^n SM_i \quad (1)$$

- the standard deviation (STD), which represents the dynamic of a SM time series:

$$\sigma = \sqrt{\frac{1}{n-1} \sum_{i=1}^n (SM_i - SM_{\text{mean}})^2} \quad (2)$$

- the coefficient of variation (CV) (Zhang et al. 2023), which characterizes the variability in changes for a SM time series:

$$CV = \frac{\sigma}{SM_{\text{mean}}} \quad (3)$$

For each site, the coefficient of variation of the *in situ* dataset remained similar before and after the temporal matching with the satellite datasets. The sites highly vary regarding climate conditions and sensor types. Their respective calibration also differ from one site to another (although ISMN tried to reach a certain consistency Dorigo et al. 2021).

The accuracy of the existing and newly developed satellite SM datasets was evaluated using four commonly used statistical indicators as defined by Gruber et al. (2020): the Root Mean Square Deviation (RMSD), the bias, the absolute bias and the Pearson correlation coefficient (R). The RMSD represents the global agreement between two time series. In this study, the RMSD was the reference metric to determine the best parameterization in our retrieval process to obtain an SM value in the A-SA, as the RMSD corresponds to a mission performance criterion (for both SMOS and SMAP). The Pearson correlation coefficient (R) represents the temporal dynamic similarities between two time series. A focus was also kept on the R that is bias insensitive and highlights the ability of a dataset to reflect the SM dynamic. The bias is the mean value of all the biases between the separate two time series. The absolute bias is the mean of the absolute values of the biases between the separate two time series.

These metrics were computed yearly for each dataset. Yearly scores then allowed obtaining the global metrics at one site. Similarly, global metrics for one SM dataset were obtained by averaging yearly scores at all sites. Note that Pearson correlation coefficient R is not an additive value. Hence, it was averaged as in Alexander (1990). The p -value was used to determine the significance level. The correlation was considered non-significant for $p > 0.05$ (Albergel et al. 2011; Gruber et al. 2020). For each satellite dataset and each year, only time series over a certain site that passed the significance test of p -value < 0.05 were kept in the analysis and used for the global metrics average.

3.3. SMOS SM inversion parameterization for A-SA environment

Our SMOS SM retrieval was based on the L-MEB which uses the $\tau - \omega$ vegetation model. In this configuration, a homogeneous vegetation layer extends over a soil layer with a rough surface. The resulting surface TB can be divided into three contributions: the soil emission attenuated by vegetation (Equation 6), the direct vegetation emission (Equation 5) and the vegetation emission reflected by the soil and then attenuated by vegetation (Equation 4). TB at a given angle of incidence (θ) and polarization ($p = H$ or $p = V$) can be written as:

$$TB_{(p,\theta)} = (1 - \omega_p)(1 - \gamma_{(p,\theta)}) T_C \gamma_{(p,\theta)} r_{G(p,\theta)} \quad (4)$$

$$+ (1 - \omega_p)(1 - \gamma_{(p,\theta)}) T_C \quad (5)$$

$$+ (1 - r_{G(p,\theta)}) \gamma_{(p,\theta)} T_G \quad (6)$$

where ω_p and $\gamma_{(p,\theta)}$ are the vegetation single scattering albedo and attenuation factor respectively, $r_{G(p,\theta)}$ is the soil reflectivity and T_C and T_G are the vegetation and soil effective temperatures. The soil effective temperature T_G was processed based on a surface temperature ($T_{\text{soil_surf}}$) and a deep temperature ($T_{\text{soil_deep}}$) according to Kerr et al. (2020):

$$T_G = T_{\text{soil_deep}} + C_t \times (T_{\text{soil_surf}} - T_{\text{soil_deep}}) \quad (7)$$

with

$$C_t = \min \left\{ \left(\frac{SM}{0.3} \right)^{0.3}, 1 \right\} \quad (8)$$

For isotropic conditions, the vegetation attenuation factor can be expressed as in Mo et al. (1982):

$$\gamma_{(\tau,\theta)} = \exp \left(\frac{-\tau}{\cos(\theta)} \right) \quad (9)$$

where τ is the optical depth at nadir (i.e. $\theta = 0^\circ$), which is independent of the polarization and the incidence angle.

The rough soil reflectivity can be empirically expressed as in J. R. Wang and Choudhury (1981):

$$r_{G(p,\theta)} = \left[(1 - Q_r) r_{G(p,\theta)}^* + Q_r r_{G(q,\theta)}^* \right] \times \exp(-H_r \cos^{N_{r(p)}}(\theta)) \quad (10)$$

where p and q are the two polarizations (q is H (resp V) when p is V (resp H)). $r_{G(p,\theta)}^*$ is the smooth soil reflectivity computed using the Fresnel equations (Ulaby, Moore, and Fung. 1981) and the soil permittivity. Besides soil moisture and temperature, the soil relative permittivity (referred to as permittivity after) depends on soil dielectric properties driven by the soil texture (sand, clay, organic content) (Mironov, Kosolapova, and Fomin 2009) (see Section 3.3.2). The soil roughness effects are taken into account with four parameters (H_r , Q_r , N_{r_h} and N_{r_v}) (J. R. Wang and Choudhury 1981) (see Section 3.3.3). Table 5 summarizes the main modeling elements of each SM dataset algorithm.

3.3.1. Water bodies

To deal with the water body fraction in the A-SA, the SMOS L3 TB were corrected for the respective open water emission before the retrieval. We tested two configurations for water fraction: either *NoWF* for which the pixel was considered homogeneous with only the main soil surface and no water body, or *WF* for which a water body fraction based on the ESA CCI land cover map was considered in the TB calculation. The total TB measured by the SMOS instrument is a weighted sum of the TB related to each class of emitters in the antenna's footprint. The water bodies' TB contribution was subtracted from the measured TB (11). Considering a certain water fraction *WF* in the

Table 5. Key components of the SM dataset algorithms for the specificities of northern A-SA.

	SMAP L3 P/PE	SMOS L2/L3	SMOS-IC	Tested models
Reference	O'Neill, Bindlish et al. (2021), Chan and Dunbar (2021)	Kerr et al. (2012), Al Bitar et al. (2017)	Wigneron et al. (2021)	– –
Soil dielectric constant	Mironov $\varepsilon_m = f(\text{SM}, T, \text{clay})$	Mironov or Bircher $\varepsilon_m = f(\text{SM}, T, \text{clay})$ $\varepsilon_b = f(\text{SM})$	Mironov $\varepsilon_m = f(\text{SM}, T, \text{clay})$	Mironov or Bircher $\varepsilon_m = f(\text{SM}, T, \text{clay})$ $\varepsilon_b = f(\text{SM})$
Soil roughness H-Q-N modeling	$H_r = f(\text{IGBP})$ Chaubell et al. (2020)	$H_r = f(\text{IGBP})$ $H_r = 0.1$ for low veg.	$H_r = f(\text{IGBP})$ $N_{th} = -1$ for low veg.	$H_r \in [0, 0.9]$ with 0.1 step
$Q_R = 0$	$N_{rh} = N_{rv} = 0$	$H_r = 0.3$ for forests $N_{rh} = 2, N_{rv} = 0$	$N_{rh} = 1$ for forests $N_{rv} = -1$	$N_{rh} = 2, N_{rv} = 0$
Single scattering albedo $\omega_H = \omega_V = \omega$	$\omega = f(\text{IGBP})$ Chaubell et al. (2020)	$\omega = f(\text{IGBP})$ $\omega = 0.08$ for low veg. $\omega = 0.06\text{--}0.08$ for forests	$\omega = f(\text{IGBP})$	$\omega \in [0, 0.14]$ with 0.01 step
Water fraction	TB correction $w\text{fraction} = f(\text{IGBP})$	fixed contribution in the inversion $w\text{fraction} = f(\text{IGBP})$	filter over 10% $w\text{fraction} = f(\text{IGBP})$	TB correction $w\text{fraction} = f(\text{CCI})$

footprint:

$$\text{TB}_{\text{waterfree}} = \frac{(\text{TB} - (\text{WF} \times \text{TB}_{\text{water}}))}{(1 - \text{WF})} \quad (11)$$

with:

$$\text{TB}_{\text{water}} = e_{\text{water}} \times T_{\text{water}} \quad (12)$$

The water emissivity e_{water} was computed as pure water emissivity (Kerr et al. 2020) and the water physical temperature T_{water} was taken from the sea surface temperature provided by the SMOS L3 TB ECMWF auxiliary data. The water fraction was extracted from the ESA CCI land cover map (ESA 2017).

3.3.2. Soil dielectric properties

The reflectivity of bare smooth soil is given by the Fresnel reflection coefficients (Ulaby, Moore, and Fung. 1981):

$$r_{G(H,\theta)}^* = \left| \frac{\cos(\theta) - \sqrt{\varepsilon_s - \sin^2(\theta)}}{\cos(\theta) + \sqrt{\varepsilon_s - \sin^2(\theta)}} \right|^2 \quad r_{G(V,\theta)}^* = \left| \frac{\varepsilon_s \cos(\theta) - \sqrt{\varepsilon_s - \sin^2(\theta)}}{\varepsilon_s \cos(\theta) + \sqrt{\varepsilon_s - \sin^2(\theta)}} \right|^2 \quad (13)$$

where ε_s is the soil permittivity – also known as the soil dielectric constant – and depends on the soil dielectric properties that are driven by the soil texture such as sand, clay and organic content.

For soils, several dielectric models at L-band – relating the dielectric constant to the soil water content – exist (Table 5). The semi-empirical Mironov dielectric model (Mironov, Kosolapova, and Fomin 2009) is based on three inputs (SM, soil effective temperature and clay content) and showed a good overall performance for SMOS (Mialon et al. 2015). The Bircher dielectric model (Bircher, Andreasen et al. 2016) was developed for organic soils, with smaller bulk densities and higher porosities that lead to higher water-holding capacities. The Bircher organic soil dielectric model uses a 3rd order polynomial in SM and results in an empirical model using no auxiliary parameters. While Bircher is specifically designed for soil with high SOC content, it performs similarly to the Mironov model for mineral soil (Bircher, Andreasen et al. 2016). In this paper, we used both Mironov and Bircher approaches (hereafter called *Mironov* and *Bircher*).

3.3.3. Soil roughness

The reflectivity of rough soil was computed from the reflectivity of bare smooth soil with four parameters to account for the soil roughness effects (Equation 10). H_r is the effective roughness parameter which is related to the spatial heterogeneity of the soil surface and spatial variations of the dielectric constant at the surface and within the soil (Escorihuela et al. 2007; Saleh et al. 2006). Q_r stands for the polarization mixing ratio (J. R. Wang et al. 1983) and N_{rh} and N_{rv} account for angular effects. As several studies suggest (Escorihuela et al. 2007; Montpetit et al. 2015), Q_r was set equal to 0. $N_{rh} = 2$ and $N_{rv} = 0$ to account for an exponentially increasing dependence of the roughness on the angle of observation for the H polarization only (Choudhury et al. 1979; J. R. Wang and Choudhury 1981). A H_r coefficient for each land cover class was usually defined in SM retrieval processes (Table 5). Besides various calibrations (Al Bitar et al. 2017; Chaubell et al. 2020; Kerr et al. 2012; Wigneron et al. 2021), the differences of N_{rh} and N_{rv} values impact the H_r values for each dataset and SMOS has a larger range of H_r values (from 0.1 to 0.3) than SMAP (from 0.11 to 0.16). For the present study, H_r values on a range of 0 to 0.9 with an iteration step of 0.1 were tested to maximize the performance over the A-SA environment.

3.3.4. Single scattering albedo

In the $\tau - \omega$ model, ω is the vegetation single scattering albedo. The dependence of ω on θ is neglected and ω currently does not have polarization dependence, i.e. $\omega_h = \omega_v = \omega$. In most retrieval processes, ω is defined as a function of the vegetation type (Table 5). SMOS L2 and L3 SM consider ω equal to 0.08 except for forests where ω is set to 0.06 or 0.08. SMOS-IC rather uses ω equal to $\simeq 0.1$ for low vegetation and ω equal to 0.06 over forests. SMAP DCA algorithm is based on Chaubell et al. (2020) calibration for each land cover class. In this study, ω values in a range of 0 to 0.14 with a 0.01 step were tested to find the best one for the A-SA environment.

3.3.5. Cost function

A 2-parameter inversion of the previously described model enabled to derive both SM and VOD by minimizing the following cost function:

$$CF = \sum \frac{(TB_{obs}(p, \theta) - TB_{sim}(p, \theta))^2}{\sigma(TB)^2} \quad (14)$$

where for both polarizations ($p = H$ and $p = V$) and at various incidence angles θ , $TB_{obs}(p, \theta)$ and $TB_{sim}(p, \theta)$ are the observed and simulated brightness temperatures respectively. $\sigma(TB)$ stands for the standard deviation of the TB and its value was set at 1.5 K for this study. Unlike Kerr et al. (2012), no additional term was considered in the cost function on the initial conditions of the derived parameters. The derived parameters are thus independent from the initial conditions. The retrieved VOD was not investigated in this study as the scope of this paper is to retrieve SM.

4. Results

4.1. SM datasets evaluation

4.1.1. Overall evaluation

A first analysis was made on the performance of each dataset over all sites from 'SpVeg', 'Shrub' and 'TreeCov' groups (Table 6). The sites from the 'HighWF' group were considered separately (see Section 4.1.2) due to the high impact of water bodies in the retrievals. The number of collocated SM observations with *in situ* SM used to compute the performance metrics is variable across the SM datasets from 1146 (SMAP L3 P PM) up to 1947 (SMOS L2 AM). The differences came from the varying satellite observations, the filtering method and the significance of test results for each dataset. AM datasets performed better than PM datasets regarding RMSD. Moreover, all datasets showed higher R values and lower bias for the AM products. The RMSD performances of all the

Table 6. SM datasets performance evaluation for both AM and PM observations against *in situ* measurements of all sites (except for the 'HighWF' group) for summertime from 2015 to 2019. For each year and each dataset, only time series that passed the significance test of p -value < 0.05 were considered. Bold data in the table highlight the values corresponding to the best result for each metric.

Dataset	RMSD ($\text{m}^3 \text{m}^{-3}$)	Bias ($\text{m}^3 \text{m}^{-3}$)	Absolute bias ($\text{m}^3 \text{m}^{-3}$)	R	Number of SM retrievals
SMOS L2 AM	0.095	-0.012	0.071	0.436	1947
SMOS L2 PM	0.100	0.033	0.075	0.398	1885
SMOS L3 AM	0.095	0.005	0.063	0.400	1900
SMOS L3 PM	0.104	0.032	0.075	0.267	1351
SMOS-IC AM	0.070	-0.003	0.051	0.501	1703
SMOS-IC PM	0.077	0.003	0.058	0.436	1521
SMAP L3 P AM	0.063	0.022	0.048	0.552	1695
SMAP L3 P PM	0.068	0.036	0.049	0.413	1146
SMAP L3 PE AM	0.066	0.021	0.050	0.554	1855
SMAP L3 PE PM	0.073	0.012	0.049	0.390	1491
CCI	0.102	0.060	0.091	0.554	1783

datasets ranged from $0.104 \text{ m}^3 \text{m}^{-3}$ (SMOS L3 PM) down to $0.063 \text{ m}^3 \text{m}^{-3}$ (SMAP L3 P AM). SMAP L3 PE AM showed a good RMSD performance ($0.066 \text{ m}^3 \text{m}^{-3}$). SMOS-IC AM ($0.070 \text{ m}^3 \text{m}^{-3}$) showed a better RMSD than SMOS-L2 AM and SMOS-L3 AM ($0.095 \text{ m}^3 \text{m}^{-3}$). CCI RMSD was higher ($0.102 \text{ m}^3 \text{m}^{-3}$) than any AM dataset. The R -value range went from 0.267 (SMOS L3 PM) up to 0.554 (SMAP L3 PE AM). SMAP L3 P AM, SMAP L3 PE AM and CCI outperformed the SMOS datasets in terms of R ($R > 0.550$). SMOS-IC AM provided the best R among the SMOS datasets ($R = 0.501$). SMOS L2 AM R (0.436) was slightly better than SMOS L3 AM R (0.400). For all PM datasets, the bias was slightly positive and lower than $0.04 \text{ m}^3 \text{m}^{-3}$, except for the CCI ($0.060 \text{ m}^3 \text{m}^{-3}$). CCI also showed the highest absolute bias ($0.091 \text{ m}^3 \text{m}^{-3}$), followed by SMOS L2 and SMOS L3 datasets ($\approx 0.070 \text{ m}^3 \text{m}^{-3}$) and SMOS-IC and SMAP datasets ($\approx 0.050 \text{ m}^3 \text{m}^{-3}$). Hence, SMAP L3 PE AM seemed to be the best overall dataset as it exhibited the best performance for the R and top performances for the RMSD and the absolute bias.

4.1.2. Site-specific evaluation

The SM measurements' variability and sensibility were characterized by the mean SM, the associated standard deviation and the coefficient of variation (CV) (Figure 2). The larger the CV, the more significant the variability in SM. Note that the mean and median values were similar for all the sites (mean difference of $0.05 \text{ m}^3 \text{m}^{-3}$). For *in situ* measurements, the mean SM value varied between the sites from $0.052 \text{ m}^3 \text{m}^{-3}$ in Mount Ryan up to $0.336 \text{ m}^3 \text{m}^{-3}$ in Daring Lake. Mount Ryan STD was

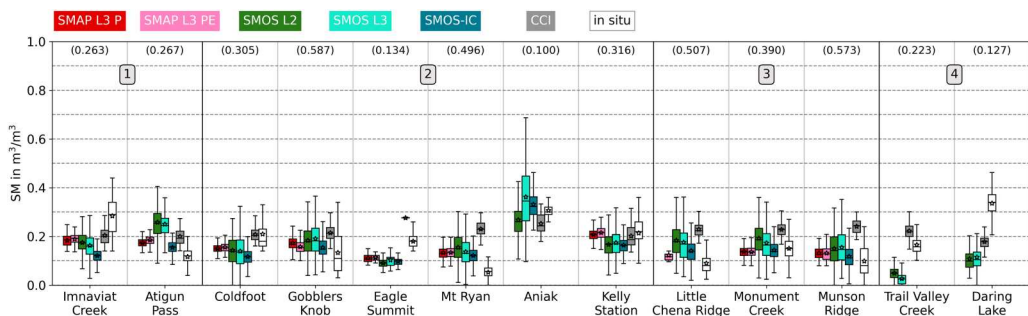


Figure 2. Site-specific characterization of the satellite products and *in situ* measurements. The box extends from the first quartile (Q1) to the third quartile (Q3) of the time series (Tukey 1977). The median is marked with a line and a star represents the mean value. The whiskers extend from $Q1 - 1.5 \times \text{IQR}$ (IQR = $Q3 - Q1$) to $Q3 + 1.5 \times \text{IQR}$. Points symbolize outliers out of the whiskers. The values in brackets on top correspond to the CV (Equation 3) of the *in situ* time series. The sites are grouped according to their land cover group: (1) *SpVeg*, (2) *Shrub*, (3) *TreeCov*, (4) *HighWF* (Table 3).

also the smallest ($0.026 \text{ m}^3 \text{ m}^{-3}$) when the highest value was reached for Gobblers Knob site ($0.078 \text{ m}^3 \text{ m}^{-3}$). The CV varied from 0.100 to 0.587. Concerning the SM satellite products, the mean SM values are in a similar range (from $0.026 \text{ m}^3 \text{ m}^{-3}$ to $0.362 \text{ m}^3 \text{ m}^{-3}$), while STD can be twice higher (up to $0.133 \text{ m}^3 \text{ m}^{-3}$ for SMOS L3 at Aniak). The SMOS SM (SMOS L2, SMOS L3 and SMOS-IC) show an STD (from $0.017 \text{ m}^3 \text{ m}^{-3}$ to $0.133 \text{ m}^3 \text{ m}^{-3}$) similar to the STD of in situ measurements (between $0.024 \text{ m}^3 \text{ m}^{-3}$ and $0.075 \text{ m}^3 \text{ m}^{-3}$) and higher than SMAP (SMAP L3 P and SMAP L3 PE) and CCI (from $0.16 \text{ m}^3 \text{ m}^{-3}$ to $0.045 \text{ m}^3 \text{ m}^{-3}$). It suggests that SMOS SM datasets better catch the SM dynamics. CCI SM mean values remain close to $0.2 \text{ m}^3 \text{ m}^{-3}$.

Further analysis of the RMSD for each AM satellite dataset over each respective site is shown in **Figure 3**. The RMSD reached at each site ranged from $0.026 \text{ m}^3 \text{ m}^{-3}$ (SMAP L3 PE at Coldfoot) to $0.155 \text{ m}^3 \text{ m}^{-3}$ (SMOS L2 at Daring Lake). Except for the high water body fraction sites (Trail Valley Creek and Daring Lake), the site-specific performances were similar to the overall performance. Similar to all site analysis, the SMAP L3 P and SMAP L3 PE yielded the best RMSD, followed by SMOS-IC, SMOS L3 and SMOS L2, while CCI RMSD exhibits high variability between the sites. The CCI product showed one of the smallest RMSD at some sites (i.e. Imnaviat Creek or Trail Valley Creek), but also the highest RMSD for the ‘*TreeCov*’ sites and some of the ‘*Shrub*’ sites (i.e. Gobblers Knob and Mount Ryan). SMAP L3 P and SMAP L3 PE RMSD were very similar for the ‘*Shrub*’ and ‘*TreeCov*’ groups. However, SMAP L3 P outperformed SMAP L3 PE for ‘*SpVeg*’. For ‘*HighWF*’ sites, SMOS-IC, SMAP L3 P and SMAP L3 PE datasets provided no SM. SMOS L2 and SMOS L3 RMSD went up to $0.243 \text{ m}^3 \text{ m}^{-3}$ while CCI dataset considerably minimized the RMSD and showed the only significant results.

4.2. SM retrievals

In our new SMOS L3 TB inversion, four configurations were tested (NoWF Mironov, NoWF Bircher, WF Mironov and WF Bircher) with the different ω and H_r combinations. The results appear as a matrix of RMSD between simulated and measured SM for each configuration. Only AM results appear here as PM has a similar behavior (as in Section 4.1), while AM showed a slightly better overall performance. In all configurations, we obtained 2530 retrievals.

4.2.1. Best configuration for the A-SA tundra

The first iterative process was performed on sites with low water fraction, i.e. removing Trail Valley Creek and Daring Lake (**Figure 4** and **Table 7**). The best RMSD between *in situ* and SMOS L3 retrieved SM was obtained without water correction using the Bircher dielectric model with the ω/H_r couple (0.08/0). Using the Mironov dielectric model, the RMSD value was minimized setting the ω/H_r couple to (0.08/0.1), also without water correction. For both Mironov and Bircher models, the water correction in the inversion process increased the RMSD. Using the Bircher model, a decrease in H_r led to decreasing errors, with the smallest RMSD for $H_r = 0$. Even if the usual

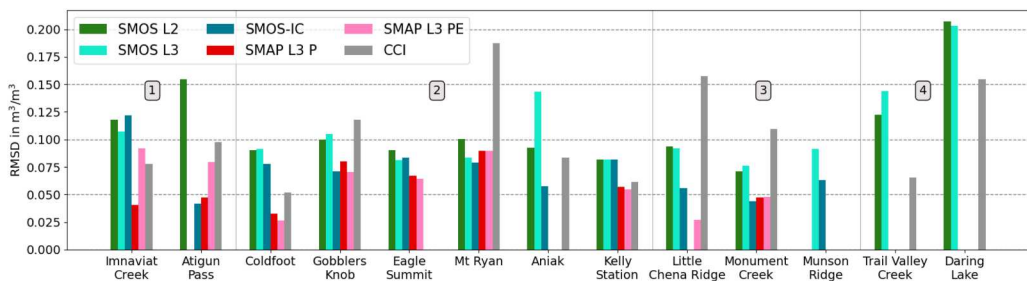


Figure 3. RMSD performance of AM satellite datasets for each site. The sites are listed according to their land cover group: (1) *SpVeg*, (2) *Shrub*, (3) *TreeCov*, (4) *HighWF* (**Table 3**).

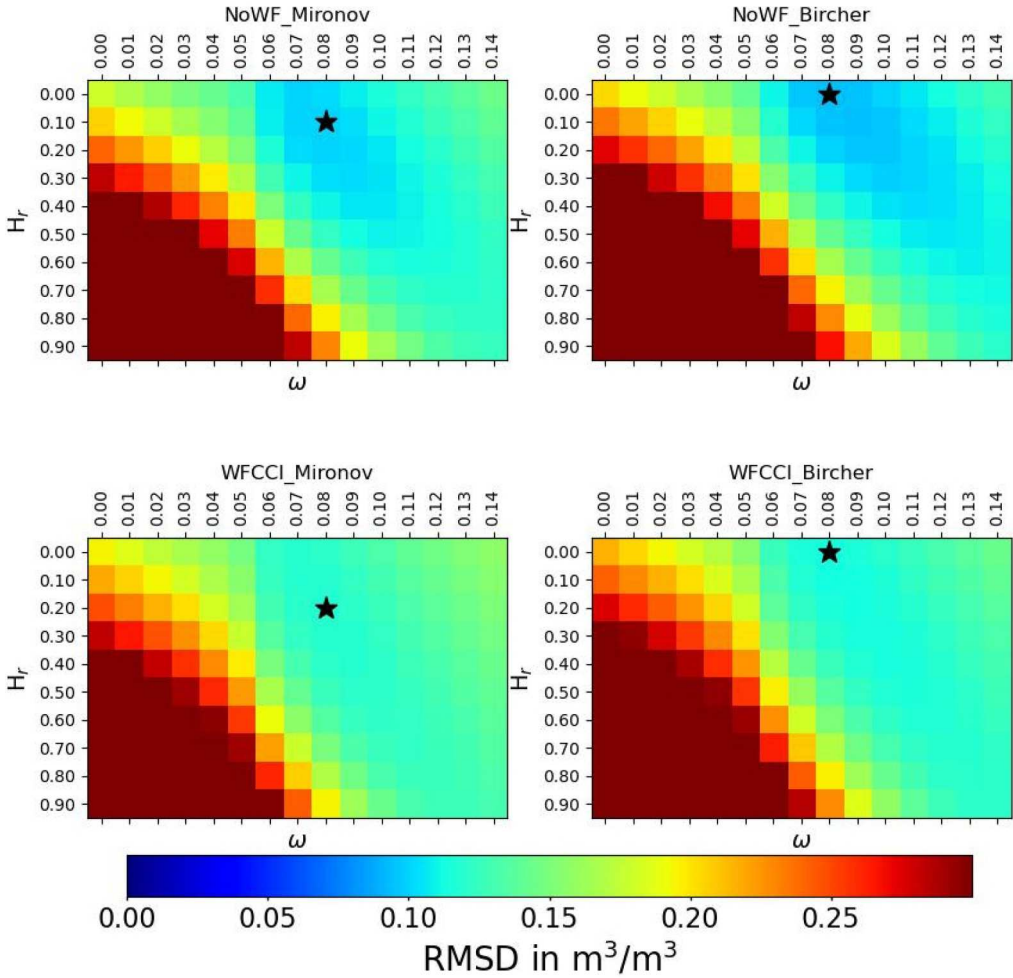


Figure 4. RMSD between *in situ* and SMOS L3 retrieved SM obtained for the four configurations, over all the sites except for the high water fraction sites Trail Valley Creek and Daring Lake. We tested different values of ω (on the horizontal axis) and of H_r (on the vertical axis). The smallest RMSD value for the configuration is symbolized with a star. The top row shows the configurations with no water correction (NoWF) and the bottom row, the configurations with water correction (WFCCI). The left column corresponds to the configuration using the Mironov dielectric model (Mironov) and the right column, the configuration using the Bircher dielectric model (Bircher).

range of H_r is between 0 and 1, H_r is actually an effective model parameter, so we extended the range of possible H to evaluate the convergence with negative H_r values. The best agreement was still obtained with $\omega = 0.08$ and $H_r = 0$. For all four configurations; it appeared that RMSD

Table 7. Best configuration performances in terms of RMSD, over all the sites except the high water fraction sites Trail Valley Creek and Daring Lake. The first two columns correspond to the configuration and the ω/H_r couple used for the inversion. The third column shows the obtained RMSD. The fourth column indicates the RMSD obtained with the ω/H_r couple (0.08/0), which was the couple finally kept in our study.

Configuration	Best (ω/H_r)	Best RMSD ($\text{m}^3 \text{m}^{-3}$)	(0.08/0) RMSD ($\text{m}^3 \text{m}^{-3}$)
NoWF Mironov	(0.08/0.1)	0.100	0.103
NoWF Bircher	(0.08/0)	0.094	0.094
WF Mironov	(0.08/0.2)	0.118	0.121
WF Bircher	(0.08/0)	0.113	0.113

Table 8. Evaluation of SMOS L3 AM retrievals using the optimal configuration (NoWF Bircher) against the *in situ* measurements over all sites for summertime from 2015 to 2019. For each year and each dataset, only time series of sites that passed the significance test of p -value < 0.05 were considered.

Dataset	RMSD ($\text{m}^3 \text{m}^{-3}$)	Bias ($\text{m}^3 \text{m}^{-3}$)	Absolute bias ($\text{m}^3 \text{m}^{-3}$)	R	Number of SM retrievals
NoWF Bircher	0.083	-0.045	0.045	0.409	1197

minimization required an $\omega > 0.05$. For higher ω , we observed a compensation effect between ω and H_r . The RMSD was effectively minimized for (0.08/0), but other ω/H_r couples led to very similar RMSD values. For the following, the selected ω/H_r couple (0.08/0) was used.

To evaluate the selected configuration (*NoWF Bircher*) in similar conditions to the other datasets (Section 4.1), we applied the same filters (e.g. TB RMSE < 8 K and p -value < 0.05). Table 8 summarizes the metrics. *NoWF Bircher* configuration showed a better RMSD than SMOS L2, SMOS L3 and CCI datasets but was still outperformed by SMOS-IC and SMAP products. The absolute bias was reduced to $0.045 \text{ m}^3 \text{m}^{-3}$ which was smaller than any other dataset, but the R was in the same range as the ones obtained with SMOS L2 and SMOS L3. The number of SM retrievals was smaller than all other AM products.

4.2.2. Selected configuration applied to each site

The best overall configuration regarding water fraction and dielectric constant (i.e. *NoWF Bircher*) was used to evaluate various ω and H_r couples for each respective site. The best (ω/H_r) pair for a site was selected following the RMSD (Table 9). For numerous sites, the best (ω/H_r) was not (0.08/0) but the RMSD value was very similar (less than $0.02 \text{ m}^3 \text{m}^{-3}$ difference). By selecting site-specific (ω/H_r) pairs, the RMSD dropped significantly (more than $0.04 \text{ m}^3 \text{m}^{-3}$) for Imnavait Creek, Atigun Pass, Eagle Summit and Daring Lake. Best ω was in a range from 0.07 to 0.014 and best H_r varied from 0 to 0.7. In this configuration, the best (ω/H_r) couple for the ‘*HighWF*’ group was (0.14/0), but with still a large RMSD.

The SM retrievals from the best overall configuration (*NoWF Bircher* (0.08/0)) and from the site-specific best configuration (*NoWF Bircher* (0.11/0.1)) were plotted together with *in situ* measurements at the Mount Ryan site for summer 2017 (Figure 5). Both of our retrievals were compared to the SM retrievals of the evaluated datasets (SMOS L2, SMOS L3, SMOS-IC, SMAP L3 P, SMAP L3 PE and CCI). The main difference between the overall and the site-specific best configurations was the time series bias. CCI performance was also characterized by a very high bias ($> 0.2 \text{ m}^3 \text{m}^{-3}$). For the other time series, differences appeared in the temporal evolution.

The best configuration regarding water fraction and dielectric constant was different from the best overall configuration only for the ‘*HighWF*’ sites, i.e. Trail Valley Creek and Daring Lake

Table 9. Best ω/H_r performance of SMOS L3 retrievals using NoWF Bircher configuration in terms of RMSD (compared to *in situ*) for each site.

Study group	Site	Best (ω/H_r)	Best RMSD ($\text{m}^3 \text{m}^{-3}$)	(0.08/0) RMSD ($\text{m}^3 \text{m}^{-3}$)	Number of SM observations
<i>SpVeg</i>	Imnavait Creek	(0.08/0.6)	0.118	0.170	321
	Atigun Pass	(0.11/0)	0.029	0.078	176
	Coldfoot	(0.08/0.5)	0.086	0.121	293
<i>Shrub</i>	Gobblers Knob	(0.11/0.4)	0.064	0.074	407
	Eagle Summit	(0.07/0.7)	0.039	0.111	22
	Mt Ryan	(0.11/0.1)	0.028	0.049	340
	Kelly Station	(0.12/0.5)	0.092	0.102	395
	Aniak	(0.08/0)	0.065	0.065	166
<i>TreeCov</i>	Little Chena Ridge	(0.08/0)	0.037	0.037	91
	Monument Creek	(0.07/0.3)	0.067	0.099	246
	Munson Ridge	(0.07/0)	0.072	0.078	73
<i>HighWF</i>	Trail Valley Creek	(0.14/0)	0.305	0.344	212
	Daring Lake	(0.14/0)	0.126	0.166	310

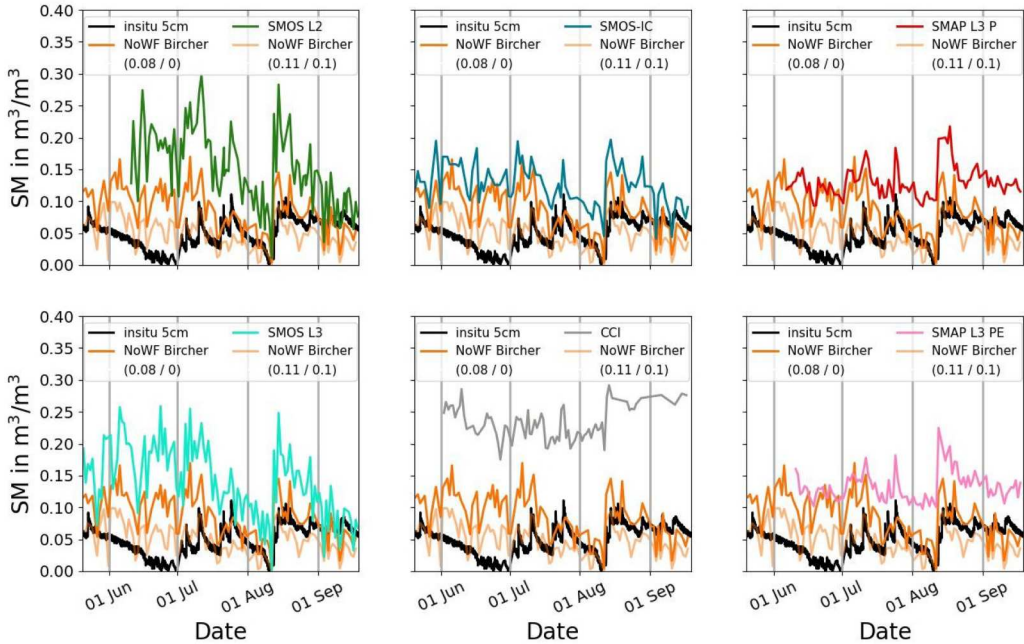


Figure 5. Time series of the SM retrievals of the evaluated AM datasets at the Mount Ryan site for summer 2017. They were compared to the *in situ* SM (black) and the SM retrieved (orange and light orange) in the inversion process proposed in this paper. The time series using the best overall configuration (0.08/0) is represented in orange and the time series using the best configuration at Mount Ryan is in light orange.

(Table 10). Surprisingly, the water fraction correction only lowered the RMSD for Trail Valley Creek. In fact, for Daring Lake, the best RMSD obtained without water correction is equal to $0.126 \text{ m}^3 \text{ m}^{-3}$ (NoWF Bircher configuration with (0.14/0)) (Table 9), whereas the best RMSD obtained with water correction is equal to $0.259 \text{ m}^3 \text{ m}^{-3}$ (WF Bircher configuration with (0.01/0.6)) (Table 10).

5. Discussion

5.1. SM datasets evaluation

Various satellite-based SM datasets were evaluated in relation to *in situ* measurements in A-SA environments. The datasets using AM satellite overpasses led to lower RMSD, lower absolute bias and higher R than when using PM orbits. The soil-canopy thermal equilibrium conditions are more easily reached in the morning (Chan and Dunbar 2021; O'Neill, Bindlish et al. 2021). The PM SM was always wetter than the AM's (at least a $0.05 \text{ m}^3 \text{ m}^{-3}$ difference of RMSD between AM and PM for each dataset). The satellite SM datasets showed a bias between $-0.10 \text{ m}^3 \text{ m}^{-3}$ and $0.10 \text{ m}^3 \text{ m}^{-3}$ yearly and at each site, which is reflected in the absolute value. Depending on the year and site, this bias can either be positive or negative leading to an average bias $\approx 0 \text{ m}^3 \text{ m}^{-3}$, showing no clear trend of the SM from the satellite datasets. For all the sites, the mean R was lower than 0.6

Table 10. Best ω/H_r performance with water fraction correction regarding RMSD for 'HighWF' group.

Study group	Site	Best (ω/H_r)	Best RMSD ($\text{m}^3 \text{ m}^{-3}$)	Number of SM observations
HighWF	Trail Valley Creek	(0.04/0.3)	0.140	212
	Daring Lake	(0.01/0.6)	0.259	310

which indicates a poor correlation with respect to R values obtained at global scale (Colliander et al. 2022). The mean RMSD for all the sites were between 0.063 and 0.104 $\text{m}^3 \text{m}^{-3}$ which was similar to the performances reached by SMAP L3 and ESA CCI datasets in the Tibetan Plateau (Zeng et al. 2022) facing similar environmental challenges. SMAP provided the best results overall and at the site-level compared to all SMOS datasets. That might be explained by a better radiometric accuracy of the instrument or the retrieval approach. The inversion process proposed in this study showed a slightly better RMSD than other SMOS datasets, but SMAP datasets still outperformed it. Contrary to the Tibetan Plateau (Liu et al. 2022; Zeng et al. 2015), the higher RMSD of the SMOS datasets seemed not to be attributable to the presence of strong RFI as they were filtered and no flags were raised. However, lower-level contamination may be present. Similarly to Zeng et al. (2015) and Zeng et al. (2022), CCI SM performance was variable depending on the site's conditions. In the ESA CCI dataset, most of the daily SM was provided from at least one passive satellite operating at L-band (SMOS or SMAP) and one passive satellite operating at C-band (Advanced Microwave Scanning Radiometer (AMSR)-2 or AMSR-E). Advanced Scatterometer (ASCAT) SM were used in the merging for some sites such as Little Chena Ridge of the 'tree covered' group and Mount Ryan which was the most vegetated of 'Shrub' sites. For both sites, the CCI dataset showed higher RMSD values than the other datasets with a variable RMSD ranging from 0.06 up to 0.13 $\text{m}^3 \text{m}^{-3}$. The merging of different sensors at various frequencies, yielding CCI results, might explain the variable performances of the CCI dataset.

Yet the emission depth and signal sensitivity vary with the wavelength. AMSR operates at several frequencies including C-band, which has a smaller emission depth than L-band and a high sensitivity to vegetation. Zwieback and Berg (2019) showed that C-band active response is highly random in tundra environments and that L-band seems more suited in such environmental conditions. Moreover, the CCI SM has the mean acquisition time of the various SM products used for computing the CCI SM. Considering this time for matching with the *in situ* measurements may lead to significant errors. Theoretically, the emission depth corresponds to 1/10 of the wavelength, i.e. 2.1 cm at L-band (Schmugge 1983). Escorihuela et al. (2010) found the best correlation between TB and SM at 0–2 cm sampling depth. However, it depends on several factors such as land cover, soil texture and SM. For wet soils, the best correlation between TB and SM was obtained at 0–1 cm (Escorihuela et al. 2010), while the best agreement was found at 2.5 cm for frozen and thawed soil on the Tibetan Plateau (Zheng et al. 2019). This variability may be a factor that leads to large differences between the *in situ* and the satellite SM datasets. The question of the effective layer to be considered at L-band in the A-SA environment should be raised. Moreover, numerous studies proved that the *in situ* instrumentation geometry (e.g. horizontal or vertical installation or type of sensor) has a huge influence on the results (Colliander et al. 2022) but is still not harmonized (Dorigo et al. 2021). Adams et al. (2015) showed that the SM vertical gradient is even stronger for high clay-content soils. Yet the typical structure in terms of soil texture in the A-SA regions is high organic content with low bulk density above a mineral layer. Consequently, the exact soil layer probed by an L-band satellite is not clearly identified. The *in situ* measurements are to be considered as a reference but they do not represent exactly what the satellite observes. Hence the target soil depth to maximize the match with *in situ* measurements remains uncertain. A similar issue concerns the effective soil temperature as it is defined (Equation 8). Both the effective soil depth definition (Equation 7) used in the algorithms and the corresponding external values used (here ECMWF temperatures) do not account for the exact sampling depth of passive microwave sensors and are approximations (Choudhury, Schmugge, and Mo 1982; Holmes et al. 2006; Wigneron, Rüdiger, and Calvet 2008). Parinussa et al. (2011) showed the impacts of the use of external temperatures on the SM retrievals at Ka-band and suggested for a similar study on associated degradations in retrieval accuracy at L-band.

Additionally, the question of the representativeness of an *in situ* probe may also be raised when evaluating a satellite product with a coarse spatial resolution (Montzka et al. 2021). Dorigo et al. (2021) assesses the representativeness errors of the ISMN data at coarse-scale (≈ 25 km) using

ECMWF Reanalysis v5 (ERA5) volumetric water content at 0–7 cm. Correcting the observed biases before the mismatch estimation enables to focus on correlation. For SNOTEL, the median representativeness error equals $0.06 \text{ m}^3 \text{ m}^{-3}$. The *in situ* sites might not represent the true value monitored by the satellite's low-resolution sensors. However, it provides useful information, especially in the singular environment of high latitudes where soil moisture datasets are to be evaluated. The resulting comparison of local probe observations to large-scale satellite data depends on the homogeneity of the area of interest (Montzka et al. 2021). The shifts in grid nodes and cell sizes between the satellite datasets may also impact the analysis. This study emphasized the issue of water bodies, particularly present in the A-SA area. Indeed, although SMAP and SMOS consider the contribution of water bodies, they fail in retrieving a reliable SM. For 'HighWF' sites, SMAP L3 P, SMAP L3 PE and SMOS-IC did not provide any SM data with sufficient retrieval quality. The RMSD of SMOS L2 and SMOS L3 reached very large values, respectively above $0.12 \text{ m}^3 \text{ m}^{-3}$ for Trail Valley Creek and above $0.20 \text{ m}^3 \text{ m}^{-3}$ for Daring Lake. These extreme RMSD values highlighted the difficulties encountered in an environment with a high water fraction, as expected by Pellarin et al. (2003). CCI dataset provided SM with lower RMSD at Trail Valley Creek ($0.065 \text{ m}^3 \text{ m}^{-3}$) than at Daring Lake ($0.155 \text{ m}^3 \text{ m}^{-3}$). Improving the impact of water bodies on L-band observations' modeling should be emphasized. However, the current modeling limitations for water bodies' areas underline the need for high-resolution products in high northern regions. Higher-resolution TB datasets could be provided by higher-resolution instruments or desegregated datasets obtained from existing data. In the SMAP case, Wrona et al. (2017) showed that using a North Polar grid with better resolution over the A-SA may be relevant.

5.2. SM retrievals

Similarly, as Zeng et al. (2015) suggested for the Tibetan Plateau environment, roughness (such as H_r) and vegetation (such as ω) parameters should be calibrated specifically for the A-SA tundra conditions. The present study showed that the ω and H_r optimized over all the study sites achieved similar performance to the best ω/H_r found for each site. Hence, keeping a single ω/H_r value seems relevant over all the A-SA areas. Further work could focus on defining a time variable ω for the A-SA region, as explored by Parinussa et al. (2018) for the Jiangxi province or by H. Wang et al. (2023) for the Amazon forest. In this study, the selected ω (0.08) is in the range of values used by the datasets evaluated (0.06–0.08), except for SMOS-IC which uses higher values (0.1–0.3). Konings et al. (2017) retrieved higher ω values from SMAP TB ($\omega > 0.17$), but warned of the water bodies and frozen season impacts in this result. Concerning the roughness parameter H_r , for all the configurations, the optimized value ($H_r = 0$) is lower than the one included in the modeling using the datasets evaluated in this study. SMOS L2, SMOS L3 and SMOS-IC have a larger range of H_r values (from 0.1 to 0.3) than SMAP L3 P and SMAP L3 PE (from 0.11 to 0.16). It may be explained by the variability of mean SM between our sites (Figure 2) as the wetter soils are more sensitive to roughness parameters as suggested by Neelam and Mohanty (2015). Finally, results showed that changes of ω and H_r parameters mostly affected the bias between the retrieved SM and the *in situ* measurements.

Regarding the L-MEB model, we tried both Mironov and Bircher dielectric models to compute the soil dielectric constant. If the Bircher dielectric constant appeared to be the most suited modeling (as expected according to Gibon et al. 2023), the impact appeared to be limited in our study. In fact, Bircher, Demontoux et al. (2016) showed that the difference between the two dielectric models increases for increasing SM ($> 0.3 \text{ m}^3 \text{ m}^{-3}$). Moreover, the calibration used for deriving the SM from the *in situ* measurements should be addressed. Organic calibration curves vary from mineral ones and lead to higher SM values (Bircher, Andreasen et al. 2016) that would affect our retrieval optimization.

Correcting the water fraction in the TB contribution as proposed in the present paper was not enough for sites with high water fraction ($> 35\%$). In that case, both H_r and ω parameters tended to compensate the water contribution with extreme values ($H_r < 0$ and $\omega > 0.12$) and the best

configuration used the Mironov dielectric constant as it tends to deliver drier retrievals. Note that neither big lakes (as at Trail Valley Creek) nor smaller water body patches (as at Daring Lake) can be handled by the tested correction. For sites with lower water fraction ($< 10\%$), applying the water fraction correction did not change the RMSD. Using high-resolution water fractions was not enough to improve the SM retrievals, but a dynamic water map could be considered as much as another modeling approach. As the water body modeling challenge is still an issue, high-resolution satellite data would be helpful in the northern A-SA to limit the number of pixels impacted by high water fraction (Rodriguez-Fernandez, Rixen, and Boutin. 2024; Rodriguez-Fernandez et al. 2022). High-resolution SM retrievals would be crucial for climate studies, as SM models also face difficulties in these regions (Andresen et al. 2020; Zwieback and Berg 2019). The SM anomalies' analysis would largely benefit from improved satellite SM products in the A-SA.

6. Conclusions

This article aims first to characterize and better describe the performance of various satellite observations to retrieve Soil Moisture over the Arctic and Sub-Arctic (A-SA) regions. We compared six satellite-derived soil moisture products over the A-SA region (SMOS L2, SMOS L3, SMOS-IC, SMAP L3 P, SMAP L3 PE and CCI). We also assessed a particular configuration to improve the satellite-derived SM obtained from the SMOS L3 TB. The evaluation was performed against *in situ* measurements over summertime over five years (2015–2019). This comparison allowed evaluating an inversion process focused on water bodies, soil dielectric constant and parametrization of ω and H_r .

Several conclusions stem from this work:

- (i) Discrepancies appear between the evaluated SM datasets. Across sites and site-specifically, SMAP provides the best SM retrievals regarding the RMSD ($< 0.07 \text{ m}^3 \text{ m}^{-3}$) and R (> 0.55).
- (ii) The applied TB correction for water body fraction appears to be insufficient to improve SM retrievals in high water fraction areas.
- (iii) The improvement related to the choice of the soil dielectric constant model is limited as both Bircher and Mironov models do yield sensible retrieval differences.
- (iv) A ω/H_r couple was optimized over all the sites (0.08/0) and was adequate over all of our study sites, which suggests that it could be applied to the entire A-SA area.

The present study shows that retrieving SM in A-SA environments from microwave satellite observations remains a significant challenge. However, this study provides some insights to improve these retrievals; they are key to better understanding the impact of climate change on these sensitive environments.

Acknowledgments

The authors are very grateful to the Centre Aval de Traitement des Données SMOS (CATDS) for providing access to the datasets and servers and to the Canadian Space Agency and the Fonds de recherche du Québec – Nature et technologies (FRQNT) for their financial support.

Data availability statement

SMOS L2 data was sourced from <https://smos-diss.eo.esa.int/oads/access/>. SMOS L3 data is openly available at <http://dx.doi.org/10.12770/9cef422f-ed3f-4090-9556-b2e895ba2ca8>. SMOS-IC data is freely available on https://data.catds.fr/cecsm/Land/_products/L3_SMOS_IC_Soil_Moisture/ SMAP L3 P and SMAP L3 PE data was sourced from <https://appears.earthdatacloud.nasa.gov/explore>. CCI data was sourced from <https://nsidc.org/data/smap/data>. ISMN data is openly available at <http://catalogue.ceda.ac.uk/uuid/ff890589c21f4033803aa550f52c980c>.


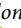



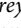
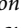
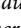



Disclosure statement

No potential conflict of interest was reported by the author(s).

Funding

This work was funded by the CNES (Centre National d'Etudes Spatiales) through J.O. PhD funding (contract no. JC.2020.OO39041) and the Science TOSCA (Terre Océan Surfaces Continentales et Atmosphère) program. The authors acknowledge the support of the Natural Sciences and Engineering Research Council of Canada (NSERC). This study has been partially supported through the grant EUR TESS N° ANR-18-EURE-0018 in the framework of the Programme des Investissements d'Avenir.

ORCID

Juliette Ortet  <http://orcid.org/0009-0002-8294-1076>
 Arnaud Mialon  <http://orcid.org/0000-0001-7970-0701>
 Yann Kerr  <http://orcid.org/0000-0001-6352-1717>
 Alain Royer  <http://orcid.org/0000-0002-6593-2007>
 Aaron Berg  <http://orcid.org/0000-0001-8438-5662>
 Julia Boike  <http://orcid.org/0000-0002-5875-2112>
 Elyn Humphreys  <http://orcid.org/0000-0002-5397-2802>
 François Gibon  <http://orcid.org/0000-0001-8656-6555>
 Philippe Richaume  <http://orcid.org/0000-0002-2945-0262>
 Simone Bircher-Adrot  <http://orcid.org/0009-0004-5668-1148>
 Azza Gorrab  <http://orcid.org/0000-0002-6870-6435>
 Alexandre Roy  <http://orcid.org/0000-0002-1472-3619>

References

- Ackerman, Daniel, Daniel Griffin, Sarah E. Hobbie, and Jacques C. Finlay. 2017. "Arctic Shrub Growth Trajectories Differ Across Soil Moisture Levels." *Global Change Biology* 23 (10): 4294–4302. <https://doi.org/10.1111/gcb.2017.23.issue-10>.
- Adams, Justin R., Heather McNairn, Aaron A. Berg, and Catherine Champagne. 2015. "Evaluation of Near-Surface Soil Moisture Data From An AAFC Monitoring Network in Manitoba, Canada: Implications for L-band Satellite Validation." *Journal of Hydrology* 521:582–592. <https://doi.org/10.1016/j.jhydrol.2014.10.024>.
- Aksoy, Mustafa, and Joel T. Johnson. 2013. "A Study of SMOS RFI Over North America." *IEEE Geoscience and Remote Sensing Letters* 10 (3): 515–519. <https://doi.org/10.1109/LGRS.2012.2211993>.
- Albergel, Clément, Elena Zakharova, Jean-Christophe Calvet, Mehrez Zribi, Mickaël Pardé, Jean-Pierre Wigneron, Nathalie Novello, et al. 2011. "A First Assessment of the SMOS Data in Southwestern France Using in Situ and Airborne Soil Moisture Estimates: The CAROLS Airborne Campaign." *Remote Sensing of Environment* 115 (10): 2718–2728. <https://doi.org/10.1016/j.rse.2011.06.012>.
- Al Bitar, Ahmad, Arnaud Mialon, Yann H. Kerr, François Cabot, Philippe Richaume, Elsa Jacqueline, Arnaud Quesney. 2017. "The Global SMOS Level 3 Daily Soil Moisture and Brightness Temperature Maps." *Earth System Science Data* 9 (1): 293–315. <https://doi.org/10.5194/essd-9-293-2017>.
- Alexander, Ralph A. 1990. "A Note on Averaging Correlations." *Bulletin of the Psychonomic Society* 28 (4): 335–336. <https://doi.org/10.3758/BF03334037>.
- Andresen, Christian G., David M. Lawrence, Cathy J. Wilson, A. David McGuire, Charles Koven, Kevin Schaefer, Elchin Jafarov. 2020. "Soil Moisture and Hydrology Projections of the Permafrost Region—A Model Intercomparison." *The Cryosphere* 14 (2): 445–459. <https://doi.org/10.5194/tc-14-445-2020>.
- Bakian-Dogahneh, Kazem, Richard H. Chen, Yonghong Yi, John S. Kimball, Mahta Moghaddam, and Alireza Tabatabaenejad. 2022. "A Model to Characterize Soil Moisture and Organic Matter Profiles in the Permafrost Active Layer in Support of Radar Remote Sensing in Alaskan Arctic Tundra." *Environmental Research Letters* 17 (2): 025011. <https://doi.org/10.1088/1748-9326/ac4e37>.
- Berg, Alexis, and Justin Sheffield. 2018. "Climate Change and Drought: The Soil Moisture Perspective." *Current Climate Change Reports* 4 (2): 180–191. <https://doi.org/10.1007/s40641-018-0095-0>.
- Bircher, Simone, Mie Andreasen, Johanna Vuollet, Juho Vehviläinen, Kimmo Rautiainen, François Jonard, Lutz Weihermüller, et al. 2016. "Soil Moisture Sensor Calibration for Organic Soil Surface Layers." *Geoscientific Instrumentation, Methods and Data Systems* 5 (1): 109–125. <https://doi.org/10.5194/gi-5-109-2016>.

- Bircher, Simone, François Demontoux, Stephen Razafindratsima, Elena Zakharova, Matthias Drusch, Jean-Pierre Wigneron, and Yann H. Kerr. 2016. "L-Band Relative Permittivity of Organic Soil Surface Layers—A New Dataset of Resonant Cavity Measurements and Model Evaluation."
- Boike, Julia, Inge Juszak, Stephan Lange, Sarah Chadburn, Eleanor Burke, Pier Paul Overduin, Kurt Roth. 2018. "A 20-Year Record (1998–2017) of Permafrost, Active Layer and Meteorological Conditions At a High Arctic Permafrost Research Site (Bayelva, Spitsbergen)." *Earth System Science Data* 10 (1): 355–390. <https://doi.org/10.5194/essd-10-355-2018>.
- Boike, Julia, Frederieke Miesner, Niko Bornemann, William L. Cable, and Inge Grünberg. 2023. "Trail Valley Creek, NWT, Canada Soil Moisture and Temperature 2016 et seq." <https://doi.org/10.1594/PANGAEA.962726>.
- Brodzik, Mary J., Brendan Billingsley, Terry Haran, Bruce Raup, and Matthew H. Savoie. 2012. "EASE-Grid 2.0: Incremental But Significant Improvements for Earth-Gridded Data Sets." *ISPRS International Journal of Geo-Information* 1 (1): 32–45. <https://doi.org/10.3390/ijgi1010032>.
- Broxton, Patrick D., Xubin Zeng, Damien Sulla-Menashe, and Peter A. Troch. 2014. "A Global Land Cover Climatology Using MODIS Data." *Journal of Applied Meteorology and Climatology* 53 (6): 1593–1605. <https://doi.org/10.1175/JAMC-D-13-0270.1>.
- Cabot, François. 2016. "CATDS-PDC L3TB – Daily Global Polarised Brightness Temperature Product from SMOS Satellite."
- CATDS. 2016. "CATDS-PDC L3SM Filtered – 1 Day Global Map of Soil Moisture Values from SMOS Satellite."
- Chan, Steven, and R. Scott Dunbar. 2021. "Enhanced Level 3 Passive Soil Moisture Product Specification Document."
- Chaubell, Mario Julian, Simon H. Yueh, R. Scott Dunbar, Andreas Colliander, Fan Chen, Steven K. Chan, Dara Entekhabi. 2020. "Improved SMAP Dual-Channel Algorithm for the Retrieval of Soil Moisture." *IEEE Transactions on Geoscience and Remote Sensing* 58 (6): 3894–3905. <https://doi.org/10.1109/TGRS.36>.
- Choudhury, B. J., T. J. Schmugge, A. Chang, and R. W. Newton. 1979. "Effect of Surface Roughness on the Microwave Emission From Soils." *Journal of Geophysical Research: Oceans* 84 (C9): 5699–5706. <https://doi.org/10.1029/JC084iC09p05699>.
- Choudhury, B. J., T. J. Schmugge, and T. Mo. 1982. "A Parameterization of Effective Soil Temperature for Microwave Emission." *Journal of Geophysical Research* 87 (C2): 1301–1304. <https://doi.org/10.1029/JC087iC02p01301>.
- Colliander, A., T. J. Jackson, S. K. Chan, P. O'Neill, R. Bindlish, M. H. Cosh, T. Caldwell. 2018. "An Assessment of the Differences Between Spatial Resolution and Grid Size for the SMAP Enhanced Soil Moisture Product Over Homogeneous Sites." *Remote Sensing of Environment* 207:65–70. <https://doi.org/10.1016/j.rse.2018.02.006>.
- Colliander, Andreas, Rolf Reichle, Wade Crow, Michael Cosh, Fan Chen, Steven Chan, Narendra Narayan Das. 2022. "Validation of Soil Moisture Data Products From the NASA SMAP Mission." *IEEE Journal of Selected Topics in Applied Earth Observations and Remote Sensing* 15:364–392. <https://doi.org/10.1109/JSTARS.2021.3124743>.
- Dorigo, Wouter, Irene Himmelbauer, Daniel Aberer, Lukas Schremmer, Ivana Petrakovic, Luca Zappa, Wolfgang Preimesberger. 2021. "The International Soil Moisture Network: Serving Earth System Science for Over a Decade." *Hydrology and Earth System Sciences* 25 (11): 5749–5804. <https://doi.org/10.5194/hess-25-5749-2021>.
- Dorigo, W., W. Preimesberger, L. Moesinger, A. Pasik, T. Scanlon, S. Hahn, R. Van der Schalie, et al. 2023. "ESA Soil Moisture Climate Change Initiative (Soil_Moisture_cci): Version 07.1 Data Collection."
- Dorigo, Wouter, Wolfgang Wagner, Clement Albergel, Franziska Albrecht, Gianpaolo Balsamo, Luca Brocca, Daniel Chung. 2017. "ESA CCI Soil Moisture for Improved Earth System Understanding: State-of-the Art and Future Directions." *Remote Sensing of Environment* 203:185–215. <https://doi.org/10.1016/j.rse.2017.07.001>.
- ESA. 2017. "ESA. Land Cover CCI Product User Guide Version 2." Tech. Rep.
- ESA. 2021. "SMOS L2 SM v700." <https://doi.org/10.57780/SM1-857C3D7>
- Escorihuela, M. J., A. Chanzy, J. P. Wigneron, and Y. H. Kerr. 2010. "Effective Soil Moisture Sampling Depth of L-band Radiometry: A Case Study." *Remote Sensing of Environment* 114 (5): 995–1001. <https://doi.org/10.1016/j.rse.2009.12.011>.
- Escorihuela, M. J., Y. H. Kerr, P. De Rosnay, J.-P. Wigneron, J.-C. Calvet, and F. Lemaitre. 2007. "A Simple Model of the Bare Soil Microwave Emission At L-Band." *IEEE Transactions on Geoscience and Remote Sensing* 45 (7): 1978–1987. <https://doi.org/10.1109/TGRS.2007.894935>.
- Falloon, Pete, Chris D. Jones, Melanie Ades, and Keryn Paul. 2011. "Direct Soil Moisture Controls of Future Global Soil Carbon Changes: An Important Source of Uncertainty: SOIL MOISTURE AND SOIL CARBON." *Global Biogeochemical Cycles* 25 (3): 1–14. <https://doi.org/10.1029/2010GB003938>.
- Gibon, François, Arnaud Mialon, Philippe Richaume, Yann H. Kerr, Nemesio J. Rodriguez-Fernandez, and Roberto Sabia. 2023. "WORK PACKAGE 5 TECHNICAL NOTE 2 SMOS VALIDATION IN ORGANIC SOIL SO-TN-CB-GS-0112 REQ-16: R&D CASE STUDY 2." (0).
- Gruber, A., G. De Lannoy, C. Albergel, A. Al-Yaari, L. Brocca, J.-C. Calvet, A. Colliander. 2020. "Validation Practices for Satellite Soil Moisture Retrievals: What Are (the) Errors?." *Remote Sensing of Environment* 244:111806. <https://doi.org/10.1016/j.rse.2020.111806>.

- Gruber, Alexander, Tracy Scanlon, Robin Van Der Schalie, Wolfgang Wagner, and Wouter Dorigo. 2019. "Evolution of the ESA CCI Soil Moisture Climate Data Records and Their Underlying Merging Methodology." *Earth System Science Data* 11 (2): 717–739. <https://doi.org/10.5194/essd-11-717-2019>.
- Holmes, T. R. H., P. de Rosnay, R. de Jeu, R. J.-P. Wigneron, Y. Kerr, J.-C. Calvet, M. J. Escorihuela, K. Saleh, and F. Lemaitre. 2006. "A New Parameterization of the Effective Temperature for L Band Radiometry." *Geophysical Research Letters* 33 (7): L07405. <https://doi.org/10.1029/2006GL025724>.
- Jackson, Thomas J., Michael H. Cosh, Rajat Bindlish, Patrick J. Starks, David D. Bosch, Mark Seyfried, David C. Goodrich, Mary Susan Moran, and Jinyang Du. 2010. "Validation of Advanced Microwave Scanning Radiometer Soil Moisture Products." *IEEE Transactions on Geoscience and Remote Sensing* 48 (12): 4256–4272. <https://doi.org/10.1109/TGRS.2010.2051035>.
- Kerr, Y. H., A. Al-Yaari, N. Rodriguez-Fernandez, M. Parrens, B. Molero, D. Leroux, S. Bircher. 2016. "Overview of SMOS Performance in Terms of Global Soil Moisture Monitoring After Six Years in Operation." *Remote Sensing of Environment* 180:40–63. <https://doi.org/10.1016/j.rse.2016.02.042>.
- Kerr, Y. H., P. Richaume, P. Waldteufel, P. Ferrazzoli, J. P. Wigneron, M. Schwank, and K. Rautiainen. 2020. "Algorithm Theoretical Basis Document (ATBD) for the SMOS Level 2 Soil Moisture Processor." *Technical Report TN-ESL-SM-GS-0001-4b SM-ESL (CBSA)* 145.
- Kerr, Y. H., F. Secherre, J. Lastenet, and J.-P. Wigneron. 2003. "SMOS: Analysis of Perturbing Effects over Land Surfaces." In *IGARSS 2003. 2003 IEEE International Geoscience and Remote Sensing Symposium. Proceedings (IEEE Cat. No.03CH37477)*, Vol. 2, Toulouse, France, 908–910. IEEE.
- Kerr, Yann H., Philippe Waldteufel, Philippe Richaume, Jean Pierre Wigneron, Paolo Ferrazzoli, Ali Mahmoodi, Ahmad Al Bitar. 2012. "The SMOS Soil Moisture Retrieval Algorithm." *IEEE Transactions on Geoscience and Remote Sensing* 50 (5): 1384–1403. <https://doi.org/10.1109/TGRS.2012.2184548>.
- Kerr, Yann H., Philippe Waldteufel, Jean-Pierre Wigneron, Steven Delwart, François Cabot, Jacqueline Boutin, Maria-José Escorihuela. 2010. "The SMOS Mission: New Tool for Monitoring Key Elements Of the Global Water Cycle." *Proceedings of the IEEE* 98 (5): 666–687. <https://doi.org/10.1109/JPROC.2010.2043032>.
- Konings, Alexandra G., Maria Piles, Narendra Das, and Dara Entekhabi. 2017. "L-Band Vegetation Optical Depth and Effective Scattering Albedo Estimation From SMAP." *Remote Sensing of Environment* 198:460–470. <https://doi.org/10.1016/j.rse.2017.06.037>.
- Lafleur, Peter M., and Elyn R. Humphreys. 2018. "Tundra Shrub Effects on Growing Season Energy and Carbon Dioxide Exchange." *Environmental Research Letters* 13 (5): 055001. <https://doi.org/10.1088/1748-9326/aab863>.
- Lawrence, D. M., C. D. Koven, S. C. Swenson, W. J. Riley, and A. G. Slater. 2015. "Permafrost Thaw and Resulting Soil Moisture Changes Regulate Projected High-Latitude CO₂ and CH₄ Emissions." *Environmental Research Letters* 10 (9): 094011. <https://doi.org/10.1088/1748-9326/10/9/094011>.
- Leavesley, George, O. David, D. C. Garen, A. G. Goodbody, J. Lea, T. Marron, T. Perkins, M. Strobel, and R. Tama. 2010. "A Modeling Framework for Improved Agricultural Water-Supply Forecasting." In *Joint Federal Interagency Hydrologic Modeling Conference*, Las Vegas, Jun.
- Liu, Weicheng, Jixin Wang, Falei Xu, Chenrui Li, and Tao Xian. 2022. "Validation of Four Satellite-Derived Soil Moisture Products Using Ground-Based In Situ Observations Over Northern China." *Remote Sensing* 14 (6): 1419. <https://doi.org/10.3390/rs14061419>.
- Lv, Shaoning, Yijian Zeng, Jun Wen, Hong Zhao, and Zhongbo Su. 2018. "Estimation of Penetration Depth From Soil Effective Temperature in Microwave Radiometry." *Remote Sensing* 10 (4): 519. <https://doi.org/10.3390/rs10040519>.
- Madelon, Remi, Nemesio J. Rodríguez-Fernández, Hassan Bazzi, Nicolas Baghdadi, Clement Albergel, Wouter Dorigo, and Mehrez Zribi. 2023. "Soil Moisture Estimates At 1 km Resolution Making a Synergistic Use of Sentinel Data." *Hydrology and Earth System Sciences* 27 (6): 1221–1242. <https://doi.org/10.5194/hess-27-1221-2023>.
- Mialon, A., L. Coret, Y. H. Kerr, F. Secherre, and J.-P. Wigneron. 2008. "Flagging the Topographic Impact on the SMOS Signal." *IEEE Transactions on Geoscience and Remote Sensing* 46 (3): 689–694. <https://doi.org/10.1109/TGRS.2007.914788>.
- Mialon, Arnaud, Philippe Richaume, Delphine Leroux, Simone Bircher, Ahmad Al Bitar, Thierry Pellarin, Jean-Pierre Wigneron, and Yann H. Kerr. 2015. "Comparison of Dobson and Mironov Dielectric Models in the SMOS Soil Moisture Retrieval Algorithm." *IEEE Transactions on Geoscience and Remote Sensing* 53 (6): 3084–3094. <https://doi.org/10.1109/TGRS.2014.2368585>.
- Mironov, V. L., L. G. Kosolapova, and S. V. Fomin. 2009. "Physically and Mineralogically Based Spectroscopic Dielectric Model for Moist Soils." *IEEE Transactions on Geoscience and Remote Sensing* 47 (7): 2059–2070. <https://doi.org/10.1109/TGRS.2008.2011631>.
- Mo, T., B. J. Choudhury, T. J. Schmugge, J. R. Wang, and T. J. Jackson. 1982. "A Model for Microwave Emission From Vegetation-Covered Fields." *Journal of Geophysical Research* 87 (C13): 11229–11237. <https://doi.org/10.1029/JC087iC13p11229>.

- Montpetit, B., A. Royer, J.-P. Wigneron, A. Chanzy, and A. Mialon. 2015. "Evaluation of Multi-Frequency Bare Soil Microwave Reflectivity Models." *Remote Sensing of Environment* 162:186–195. <https://doi.org/10.1016/j.rse.2015.02.015>.
- Montzka, Carsten, Michael Cosh, Jaime Nickeson, and Fernando Camacho. 2021. "Soil Moisture Product Validation Good Practices Protocol."
- Myers-Smith, Isla H., Jeffrey T. Kerby, Gareth K. Phoenix, Jarle W. Bjerke, Howard E. Epstein, Jakob J. Assmann, Christian John. 2020. "Complexity Revealed in the Greening of the Arctic." *Nature Climate Change* 10 (2): 106–117. <https://doi.org/10.1038/s41558-019-0688-1>.
- Naeimi, V., K. Scipal, Z. Bartalis, S. Hasenauer, and W. Wagner. 2009. "An Improved Soil Moisture Retrieval Algorithm for ERS and METOP Scatterometer Observations." *IEEE Transactions on Geoscience and Remote Sensing* 47 (7): 1999–2013. <https://doi.org/10.1109/TGRS.2008.2011617>.
- Neelam, Maheshwari, and Binayak P. Mohanty. 2015. "Global Sensitivity Analysis of the Radiative Transfer Model." *Water Resources Research* 51 (4): 2428–2443. <https://doi.org/10.1002/wrcr.v51.4>.
- Ochsner, Tyson E., Michael H. Cosh, Richard H. Cuenca, Wouter A. Dorigo, Clara S. Draper, Yutaka Hagimoto, Yann H. Kerr. 2013. "State of the Art in Large-Scale Soil Moisture Monitoring." *Soil Science Society of America Journal* 77 (6): 1888–1919. <https://doi.org/10.2136/sssaj2013.03.0093>.
- O'Neill, Peggy, Rajat Bindlish, Steven Chan, Julian Chaubell, Andreas Colliander, Eni Njoku, and Tom Jackson. 2021. "Algorithm Theoretical Basis Document Level 2 & 3 Soil Moisture (Passive) Data Products."
- O'Neill, Peggy E., Steven Chan, Eni G. Njoku, Tom Jackson, Rajat Bindlish, and M. Julian Chaubell. 2021. "SMAP L3 Radiometer Global Daily 36 km EASE-Grid Soil Moisture, Version 8." Accessed Novemembr 19, 2023. <https://nsidc.org/data/spl3smp/versions/8>.
- O'Neill, Peggy E., Steven Chan, Eni G. Njoku, Tom Jackson, Rajat Bindlish, M. Julian Chaubell, and Andreas Colliander. 2021. "SMAP Enhanced L3 Radiometer Global and Polar Grid Daily 9 km EASE-Grid Soil Moisture, Version 5." Accessed November 19, 2023. https://nsidc.org/data/spl3smp_e/versions/5.
- Owe, Manfred, Richard De Jeu, and Thomas Holmes. 2008. "Multisensor Historical Climatology of Satellite-Derived Global Land Surface Moisture." *Journal of Geophysical Research: Earth Surface* 113 (F1): 2007JF000769. <https://doi.org/10.1029/2007JF000769>.
- Parinussa, R. M., T. R. H. Holmes, M. T. Yilmaz, and W. T. Crow. 2011. "The Impact of Land Surface Temperature on Soil Moisture Anomaly Detection From Passive Microwave Observations." *Hydrology and Earth System Sciences* 15 (10): 3135–3151. <https://doi.org/10.5194/hess-15-3135-2011>.
- Parinussa, Robert Mathijs, Guojie Wang, Yi Liu, Dan Lou, Daniel Fiifi Tawia Hagan, Mingjin Zhan, Buda Su, and Tong Jiang. 2018. "Improved Surface Soil Moisture Anomalies From Fengyun-3B Over the Jiangxi Province of the People's Republic of China." *International Journal of Remote Sensing* 39 (23): 8950–8962. <https://doi.org/10.1080/01431161.2018.1500729>.
- Pekel, Jean-François, Andrew Cottam, Noel Gorelick, and Alan S. Belward. 2016. "High-Resolution Mapping of Global Surface Water and Its Long-Term Changes." *Nature* 540 (7633): 418–422. <https://doi.org/10.1038/nature20584>.
- Pellarin, Thierry, Jean-Pierre Wigneron, Jean-Christophe Calvet, and Philippe Waldteufel. 2003. "Global Soil Moisture Retrieval from a Synthetic L-band Brightness Temperature Data Set." *Journal of Geophysical Research: Atmospheres* 108 (D12): 2002JD003086. <https://doi.org/10.1029/2002JD003086>.
- Poggio, Laura, Luis M. De Sousa, Niels H. Batjes, Gerard B. M. Heuvelink, Bas Kempen, Eloi Ribeiro, and David Rossiter. 2021. "SoilGrids 2.0: Producing Soil Information for the Globe with Quantified Spatial Uncertainty." *Soil* 7 (1): 217–240. <https://doi.org/10.5194/soil-7-217-2021>.
- Rawls, W. J., Y. A. Pachepsky, J. C. Ritchie, T. M. Sobecki, and H. Bloodworth. 2003. "Effect of Soil Organic Carbon on Soil Water Retention." *Geoderma* 116 (1-2): 61–76. [https://doi.org/10.1016/S0016-7061\(03\)00094-6](https://doi.org/10.1016/S0016-7061(03)00094-6).
- Rodriguez-Fernandez, N. J., E. Anterrieu, J. Boutin, A. Supply, G. Reverdin, G. Alory, E. Remy, et al. 2022. "The SMOS-HR Mission: Science Case and Project Status." In *IGARSS 2022 – 2022 IEEE International Geoscience and Remote Sensing Symposium*, Kuala Lumpur, Malaysia, Jul., 7182–7185. IEEE.
- Rodriguez-Fernandez, N., T. Rixen, and Jacqueline Boutin. 2024. "The Fine Resolution Explorer for Salinity, Carbon and Hydrology (FRESCHE). A Mission to Study Ocean-Land-Ice Interfaces (submitted)." In *IGARSS 2024 -- 2024 IEEE International Geoscience and Remote Sensing Symposium*.
- Saleh, Kauzar, Jean-Pierre Wigneron, Patricia De Rosnay, Jean-Christophe Calvet, and Yann Kerr. 2006. "Semi-Empirical Regressions At L-band Applied to Surface Soil Moisture Retrievals Over Grass." *Remote Sensing of Environment* 101 (3): 415–426. <https://doi.org/10.1016/j.rse.2006.01.008>.
- Schmugge, Thomas J. 1983. "Remote Sensing of Soil Moisture: Recent Advances." *IEEE Transactions on Geoscience and Remote Sensing GE-21* (3): 336–344. <https://doi.org/10.1109/TGRS.1983.350563>.
- Seneviratne, Sonia I., Thierry Corti, Edouard L. Davin, Martin Hirschi, Eric B. Jaeger, Irene Lehner, Boris Orłowski, and Adriaan J. Teuling. 2010. "Investigating Soil Moisture–Climate Interactions in a Changing Climate: A Review." *Earth-Science Reviews* 99 (3-4): 125–161. <https://doi.org/10.1016/j.earscirev.2010.02.004>.

- Talone, M., M. Portabella, J. Martinez, and V. Gonzalez-Gambau. 2015. "About the Optimal Grid for SMOS Level 1C and Level 2 Products." *IEEE Geoscience and Remote Sensing Letters* 12 (8): 1630–1634. <https://doi.org/10.1109/LGRS.2015.2416920>.
- Tukey, John W. 1977. *Exploratory Data Analysis. Behavioral Science: Quantitative Methods*. 1st ed. Boston: Addison-Wesley.
- Ulaby, F. T., R. K. Moore, and A. K. Fung. 1981. *Microwave Remote Sensing – Active and Passive*. Vol. I, II, III. Norwood, MA: Addison-Wesley Publishing Company, Artech House.
- Wagner, W., W. Dorigo, R. De Jeu, D. Fernandez, J. Benveniste, E. Haas, and M. Ertl. 2012. "Fusion of Active and Passive Microwave Observations to Create An Essential Climate Variable Data Record on Soil Moisture." *ISPRS Annals of the Photogrammetry, Remote Sensing and Spatial Information Sciences* I-7:315–321. <https://doi.org/10.5194/isprsannals-I-7-315-2012>.
- Wagner, Wolfgang, Guido Lemoine, and Helmut Rott. 1999. "A Method for Estimating Soil Moisture From ERS Scatterometer and Soil Data." *Remote Sensing of Environment* 70 (2): 191–207. [https://doi.org/10.1016/S0034-4257\(99\)00036-X](https://doi.org/10.1016/S0034-4257(99)00036-X).
- Wang, J. R., and B. J. Choudhury. 1981. "Remote Sensing of Soil Moisture Content, Over Bare Field At 1.4 GHz Frequency." *Journal of Geophysical Research* 86 (C6): 5277–5282. <https://doi.org/10.1029/JC086iC06p05277>.
- Wang, James R., Peggy E. O'Neill, Thomas J. Jackson, and Edwin T. Engman. 1983. "Multifrequency Measurements of the Effects of Soil Moisture, Soil Texture, And Surface Roughness." *IEEE Transactions on Geoscience and Remote Sensing* GE-21 (1): 44–51. <https://doi.org/10.1109/TGRS.1983.350529>.
- Wang, Huan, Jean-Pierre Wigneron, Philippe Ciais, Yitong Yao, Lei Fan, Xiangzhuo Liu, Xiaojun Li. 2023. "Seasonal Variations in Vegetation Water Content Retrieved From Microwave Remote Sensing Over Amazon Intact Forests." *Remote Sensing of Environment* 285:113409. <https://doi.org/10.1016/j.rse.2022.113409>.
- Wigneron, Jean-Pierre, Xiaojun Li, Frédéric Frappart, Lei Fan, Amen Al-Yaari, Gabrielle De Lannoy, Xiangzhuo Liu, et al. 2021. "SMOS-IC Data Record of Soil Moisture and L-VOD: Historical Development, Applications and Perspectives." *Remote Sensing of Environment* 254:112238. <https://doi.org/10.1016/j.rse.2020.112238>.
- Wigneron, Jean-Pierre, Christoph Rüdiger, and Jean-Christophe Calvet. 2008. "Estimating the Effective Soil Temperature At L-Band As a Function of Soil Properties." *IEEE Transactions on Geoscience and Remote Sensing* 46 (3): 797–807. <https://doi.org/10.1109/TGRS.2007.914806>.
- Wrona, Elizabeth, Tracy L. Rowlandson, Manoj Nambiar, Aaron A. Berg, Andreas Colliander, and Philip Marsh. 2017. "Validation of the Soil Moisture Active Passive (SMAP) Satellite Soil Moisture Retrieval in An Arctic Tundra Environment." *Geophysical Research Letters* 44 (9): 4152–4158. <https://doi.org/10.1002/grl.v44.9>.
- Yi, Yonghong, Richard H. Chen, John S. Kimball, Mahta Moghaddam, Xiaolan Xu, Eugénie S. Euskirchen, Narendra Das, and Charles E. Miller. 2022. "Potential Satellite Monitoring of Surface Organic Soil Properties in Arctic Tundra From SMAP." *Water Resources Research* 58 (4): e2021WR030957. <https://doi.org/10.1029/2021WR030957>.
- Zeng, Jiangyuan, Zhen Li, Quan Chen, Haiyun Bi, Jianxiu Qiu, and Pengfei Zou. 2015. "Evaluation of Remotely Sensed and Reanalysis Soil Moisture Products Over the Tibetan Plateau Using In-Situ Observations." *Remote Sensing of Environment* 163:91–110. <https://doi.org/10.1016/j.rse.2015.03.008>.
- Zeng, Jiangyuan, Pengfei Shi, Kun-Shan Chen, Hongliang Ma, Haiyun Bi, and Chenyang Cui. 2022. "Assessment and Error Analysis of Satellite Soil Moisture Products Over the Third Pole." *IEEE Transactions on Geoscience and Remote Sensing* 60:1–18.
- Zhang, Peng, Hongbo Yu, Yibo Gao, and Qiaofeng Zhang. 2023. "Evaluation of Remote Sensing and Reanalysis Products for Global Soil Moisture Characteristics." *Sustainability* 15 (11): 9112. <https://doi.org/10.3390/su15119112>.
- Zheng, Donghai, Xin Li, Xin Wang, Zuoliang Wang, Jun Wen, Rogier Van Der Velde, Mike Schwank, and Zhongbo Su. 2019. "Sampling Depth of L-band Radiometer Measurements of Soil Moisture and Freeze-Thaw Dynamics on the Tibetan Plateau." *Remote Sensing of Environment* 226:16–25. <https://doi.org/10.1016/j.rse.2019.03.029>.
- Zona, Donatella, Peter M. Lafleur, Koen Hufkens, Beniamino Gioli, Barbara Bailey, George Burba, Eugénie S. Euskirchen. 2023. "PAN-ARCTIC Soil Moisture Control on Tundra Carbon Sequestration and Plant Productivity." *Global Change Biology* 29 (5): 1267–1281. <https://doi.org/10.1111/gcb.v29.5>.
- Zwieback, Simon, and Aaron A. Berg. 2019. "Fine-Scale SAR Soil Moisture Estimation in the Subarctic Tundra." *IEEE Transactions on Geoscience and Remote Sensing* 57 (7): 4898–4912. <https://doi.org/10.1109/TGRS.36>.

Appendix. For 'HighWF' sites

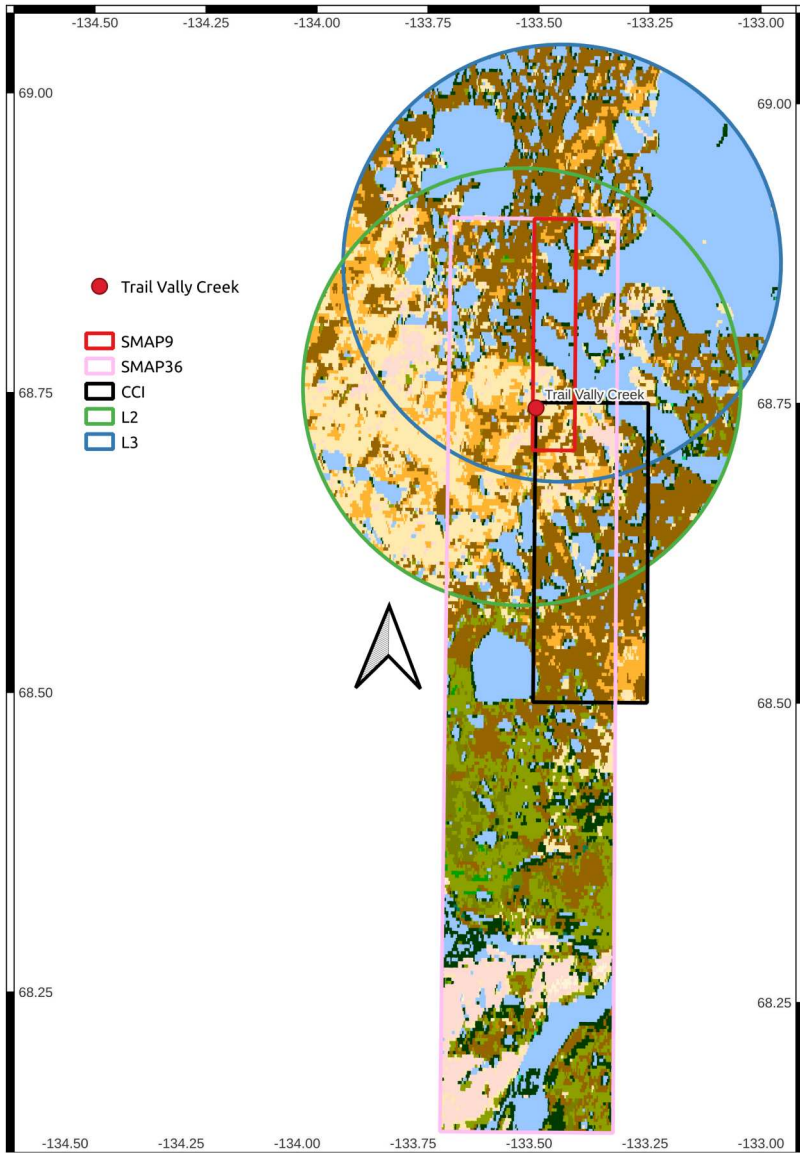


Figure A1. Approximated field of view considered by each satellite product at Trail Valley Creek (background: ESA CCI L4 map at 300 m, Version 2.0.7 (2015) ESA 2017). The *in situ* measurements station is symbolized by a red point.

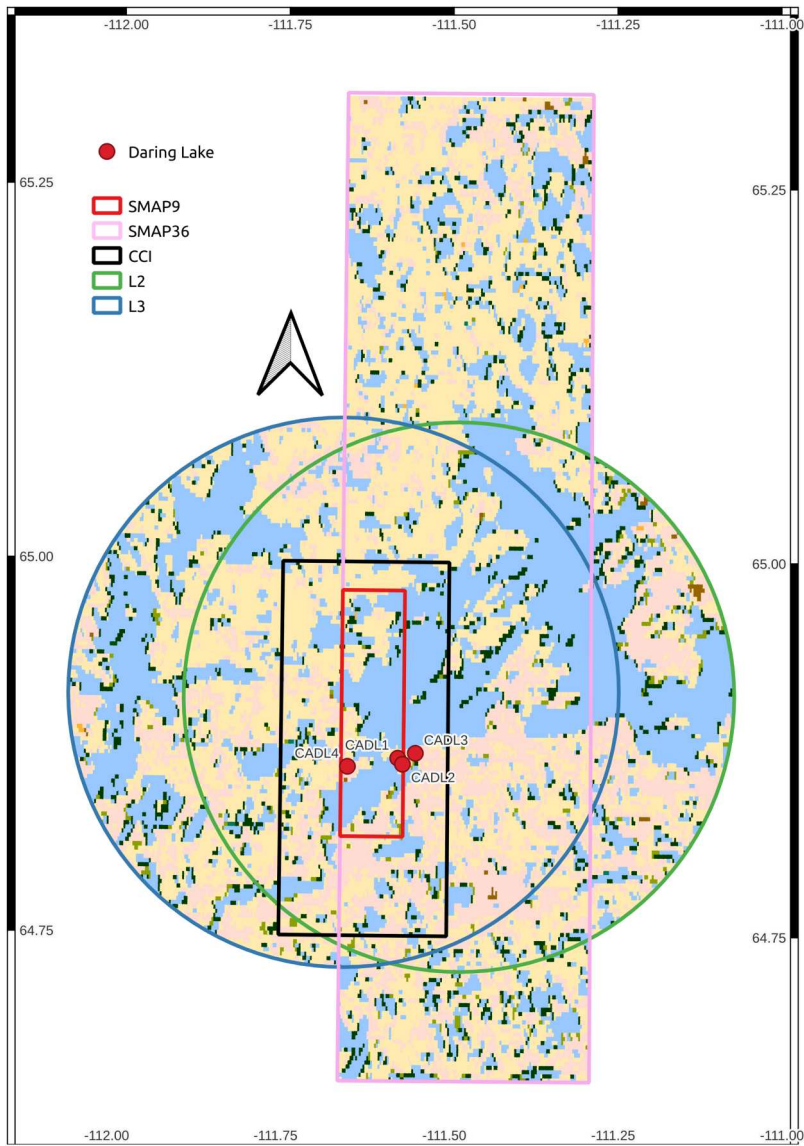


Figure A2. Approximated field of view considered by each satellite product at Daring Lake (background: ESA CCI L4 map at 300 m, Version 2.0.7 (2015) ESA 2017). The *in situ* measurements stations are symbolized by a red point.